CLAS12 Run-group H Experiments with a Transversely Polarized Target

Contents

Abstract

We propose an optimized experimental configuration to meet the goals of three C2 conditionally approved CLAS12 deep-inelastic scattering (DIS) experiments with a transversely polarized target, identified as run-group H. The usage of a transversely polarized Hydrogen target in conjunction with the CLAS12 spectrometer and an 11 GeV polarized electron beam will provide access to unique aspects of nucleon structure at the scale of confinement. In particular, the experiments of RGH will measure transverse target single- and double-spin asymmetries in semi-inclusive and hard-exclusive reactions to chase some of the most elusive and peculiar parton distribution and correlation functions among the transverse momentum dependent (TMDs) and generalized (GPDs) distributions.

C12-11-111 will study the semi-inclusive reaction $ep^{\uparrow} \rightarrow ehX$, (with h an identified hadron and X the undetected final state), to access leading-twist parton distribution functions in a transversely polarized nucleon. The transversity, the Sivers function and the so-called "pretzelosity" function describe the correlation between the transverse nucleon polarization and, respectively, the transverse polarization of partons, the transverse momentum of unpolarized partons and the transverse momentum of transversely polarized partons. Furthermore, double-spin asymmetries based on both the target transverse and the beam longitudinal polarizations will provide access to the so-called "worm-gear" function, sensitive to the correlation between the transverse momentum of longitudinally polarized partons and the nucleon transverse polarization. RGH data will also provide constraints to the transverse-momentum dependent Collins fragmentation function.

C12-12-009 will study the semi-inclusive reaction $ep^{\uparrow} \rightarrow eh_1h_2X$ (with h_1 and h_2 two identified final state hadrons) to access the transversity distribution and its first moment, the tensor charge, in a reaction that can be described by a standard collinear formalism and provides a benchmark for the alternate transverse-momentum dependent (TMD) extraction.

C12-12-010 will measure the deeply virtual Compton scattering (DVCS) on the proton, $ep^{\uparrow} \rightarrow ep\gamma$, whose azimuthal spin asymmetries depend on combinations of Generalized Parton distributions (GPDs), to provide access to the elusive and poorly constrained GPD E. E is the missing ingredient to quantify the quarks' orbital momentum contribution to the proton spin. Only the transverse-target spin asymmetry of DVCS has a strong sensitivity to the E GPD of the proton, and so far it has been measured only by HERMES, on a limited kinematic coverage and with very poor statistics. RGH will measure also double-spin asymmetries for proton DVCS, giving access to the real part of the target-spin dependent DVCS amplitude.

This set of experiments will contribute to a comprehensive investigation of nucleon structure in the CEBAF energy domain performed with the same spectrometer. The x, Q^2, z, P_{hT} dependencies will be studied in a wide kinematic range thanks to the large acceptance of CLAS12. Flavor sensitivity will be ensured by the available excellent particle identification systems.

In order to allow a multi-dimensional analysis to disentangle the relevant kinematic correlations in an uneplored region of valence, be competitive with lattice calculations on the u-flavor tensor charge, and provide relevant constraints to the GPD E, a total of 125 PAC days are requested, including 25 PAC days of commissioning, calibration and target operations, and 100 PAC days of production data taking.

1 Executive Summary

The CLAS12 run-group H (RGH) comprises 3 experiments, requiring a transversely polarized target, originally approved with rating A by PAC39 [1] and selected among the high-impact JLab measurements by PAC41 [2]:

- **C12-11-111** *Transverse spin effects in SIDIS at 11 GeV with a transversely polarized target using CLAS12*: a multi-dimensional analysis of the semi-inclusive deep-inelastic scattering (SIDIS) reactions to access transversity and tensor charge, and the Sivers and Collins functions connected with the spin-orbit phenomena of the strong-force dynamics [3];
- **C12-12-009** *Measurement of transversity with dihadron production in SIDIS with transversely polarized target*: a multi-dimensional analysis of the SIDIS reactions at 11 GeV exploiting the dynamics of the dihadron final state to access transversity in the benchmark collinear limit and investigate novel parton correlations inaccessible on the single hadron case [4];
- **C12-12-010** *Deeply Virtual Compton Scattering at 11 GeV with transversely polarized target using the CLAS12 Detector*: a first-time multi-dimensional extraction of the transverse target spin asymmetry for the DVCS reaction to access E, the most elusive Generalized Parton Distribution entering the orbital momentum sum rule (Ji sum rule) [5].

The RGH experiments pursue a science case of utmost interest as highlighted in the current 2023 NSAC Long Range Plan. They will have a strong sensitivity to several crucial observables whose current knowledge is severely limited by the sparse data available. The RGH experiments are a precursor and complementary to one of the pillars of the EIC science programs [6, 7] and will cover the valence phase space with unprecedented precision. RGH program completes a comprehensive study of all possible target and beam polarizations with the existing CLAS12 large-acceptance spectrometer. Distinctive features, common to all the three RGH experiments, are the precise measurement of parton distributions and phenomena in an unexplored valence region where current models project their magnitude to be peaking, a luminosity at least one order of magnitude higher than the previous experiments, a large acceptance detector for the disentanglement of the various correlations and kinematic regimes, and an excellent particle identification capability to access flavor sensitivity.

All three experiments received a C1 condition to address technical issues related to target performance. The eventually adopted solution foresees a dynamically polarized NH_3 target with a dedicated recoil detector replacing the CLAS12 solenoid and Central Detector. Such a solution favors consolidated polarized-target technologies and relies on previous successful realizations at JLab. During the jeopardy process at PAC52, RGH status changed to a C2 condition to assess in more details the revised experimental configuration, in particular regarding the achievable physics impact in conjunction with the required beamtime [8]. The specific requests of PAC52 have been addressed here:

- a full GEANT simulation of the beamline is discussed in Section 4.2;
- a full GEANT simulation of the different physics measurement is discussed in Section 4.3.3;

- the systematic uncertainties for the different measurements are discussed in Section 6.3;
- impact studies of the measurements on the physics observables are presented in Section 6.1 and 6.2.

The achievable luminosity is defined by the background level in the detector and the nominal $\mathcal{L} = 5 \times 10^{33}$ cm^{-2}s^{-1} RGH value corresponds to the most realistic (based on real-data) and conservative (based on present CLAS12 capability without ongoing upgrades) estimate and requires a modest beam current of O(1) nA. In order to be competitive with lattice calculations on the u-flavor tensor charge, and provide relevant constraints to the GPD E, a total of 125 PAC days are requested, including 25 PAC days of commissioning, calibration and target operations, and 100 PAC days of production data taking.

2 Physics Motivation

In recent years, new parton distributions (PDFs) and fragmentation functions (FFs) have been introduced to describe the rich complexity of hadron structure, focusing on the parton transverse degrees of freedom at the scale of confinement and moving toward the achievement of a 3D description of parton dynamics. Relevant examples are transverse momentum dependent (TMD) and generalized (GPD) parton distributions, relating the longitudinal momentum fraction (referred to the direction of the hard probe) with the intrinsic partonic transverse momentum or position, respectively. These novel distribution functions can be classified depending on the spin orientation of the target nucleon and quark, as these dictates the type of underneath correlation, see Figure 1.

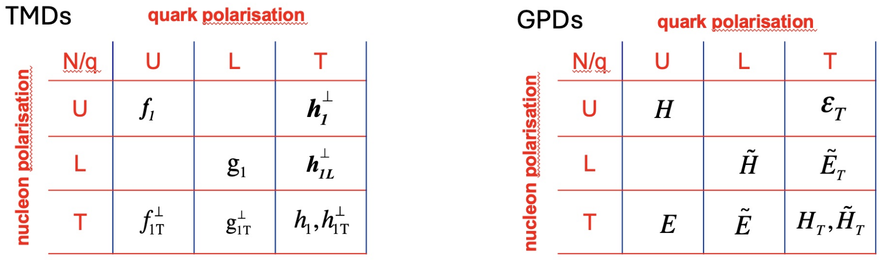

TMDs

quark polarisation

nucleon polarisation

N/q	U	L	T
U	f_1		$h_1^\perp$
L		g_1	$h_{1L}^\perp$
T	$f_{1T}^\perp$	$g_{1T}^\perp$	$h_1, h_{1T}^\perp$

GPDs

quark polarisation

nucleon polarisation

N/q	U	L	T
U	H		$\mathcal{E}_T$
L		$\tilde{H}$	$\tilde{E}_T$
T	E	$\tilde{E}$	$H_T, \tilde{H}_T$

Fig. 1: TMD and GPD classification based on the relevant spin (target nucleon or quark) orientation.

Because TMDs and GPDs are derived by integrations of distinctive components of the 5-dimensional Wigner functions [9], the most general parton distribution functions, they are formally independent. Nevertheless, intriguing model-dependent relations can be found among them. An interesting example is the possible relationship between the TMD Sivers function $f_{1T}^\perp$ and GPD E. The Sivers function is related to the distortion in the momentum distribution of an unpolarized parton when the parent nucleon is transversely polarized. The GPD E enters the Ji sum rule for the longitudinal angular momentum and describes an imbalance in the impact parameter space of the quarks in reactions with nucleon helicity flip, but unaffected quark helicity. The two can be related by the so-called lensing mechanism, inspired by results of spectator models and described by a flavor-indepedent function, representing the effect of the QCD interaction of the outgoing quark with the rest of the nucleon [10]. This relationship has been used to infer constraints on the quark angular momenta [11]

TMDs can be measured in polarized semi-inclusive DIS (SIDIS) reactions, where the leading hadron is measured in conjunction with the scattered lepton. The SIDIS cross-sections can be Fourier decomposed into terms that depend on beam λ_e and target $S_{L,T}$ polarizations:

$$\frac{d\sigma_{UT}}{dxdQ^2dzdP_{h\perp}d\phi d\phi_S} \propto \left[F_{UU} + \epsilon\cos(\phi)F_{LU}^{\cos(2\phi)}\right] + \mathrm{S}_L\left[\sin(2\phi)F_{LU}^{\sin(2\phi)}\right] +$$

$$S_T\left[\sin(\phi-\phi_S)\,F_{UT}^{\sin(\phi-\phi_S)} + \epsilon\sin(\phi+\phi_S)\,F_{UT}^{\sin(\phi+\phi_S)} + \epsilon\sin(3\phi-\phi_S)\,F_{UT}^{\sin(3\phi-\phi_S)}\right]$$

$$+\lambda_e S_L \left[\sqrt{1-\epsilon^2} F_{LL}\right] \; + \; \lambda_e S_T \left[\sqrt{1-\epsilon^2}\cos(\phi-\phi_S)\, F_{LT}^{\cos(\phi-\phi_S)}\right] + O(1/Q^2)$$

where the cross-section depends on the Bjorken x, the photon virtuality Q^2, the hadron energy fraction z and hadron transverse momentum $P_{h\perp}$, the azimuthal angles ϕ and ϕ_S of the produced hadron and target spin with respect to the lepton scattering plane, respectively. Polarization prefactors depend on the ratio ϵ of longitudinal and transverse photon flux. Each term has a distinctive modulation in the azimuthal angles and contains a structure function F_{XY} with subscripts XY indicating the beam and target polarization. Within TMD factorization, each structure function can be interpreted as a convolution of a parton distribution and fragmentation function, e.g.:

$$F_{UU} = C\left[f_1(x, k_T) \times D_1(z, p_T)\right]$$

where the convolution

$$C = x \sum_q e_q^2 \int d^2p_T\, d^2k_T\; \delta(P_{h\perp} - zk_T - p_T)\; w(k_T, p_T)\; f_1^q(x, k_T) D_1^q(z, p_T)$$

runs over the intrinsic transverse momentum k_T of the parton and the transverse momentum p_T generated during fragmentation. The delta function δ ensures the conservation of momentum for the observed transverse momentum $P_{h\perp}$, and the weight function w is a calculable kinematic factor.

Exploring parton correlations at the confined scale is a formidable challenge. The peculiar nature of the strong force, which favors multi-body interactions, is reflected in a complex variety of possible correlations and requires the capability to explore large portions of the phase space and disentangle various kinematic dependencies. This can be ultimately achieved only by collecting observables from all the possible reactions, typically deep-inelastic scattering, Drell-Yan, e^+e^- annihilation, and hadron-hadron interactions, investigated in various facilities over the world.

Deep-inelastic scattering (DIS) experiments play a special role, thanks to clean control of the probe kinematics and rich phenomenology, which convolutes parton distributions and fragmentation functions. A novel level of sophistication is required to the DIS experiments as they should conjugate precision, in discriminating semi-inclusive and exclusive reaction details and hadron species, and power, in collecting large amounts of data to allow multi-dimensional analyses. The investigation of the non-perturbative parton dynamics typically requires two scales: a hard scale defining the DIS regime and a soft scale accessing the confined dynamics. The first scale is associated with the virtual photon 4-momentum Q. The second is associated with the intrinsic momentum $k_\perp$ of the partons (in the case of TMDs) or with the momentum transferred t to the unbroken target nucleon (in the case of GPDs). Note that the hard scale should be larger than the soft scale to allow proper factorization, but not too large to avoid an overwhelming dilution via perturbative radiation effects (in the case of semi-inclusive reactions) or unnecessary cross-section suppression (in the case of exclusive reactions).

Fixed-target DIS experiments have played an essential role despite the limited statistics accumulated so far. The CLAS12 run-group H program aims to collect several fundamental measurements that provide access to elusive quantities and are only possible with the use of a transversely polarized target in conjunction with a high-precision spectrometer of large acceptance and unprecedented luminosity.

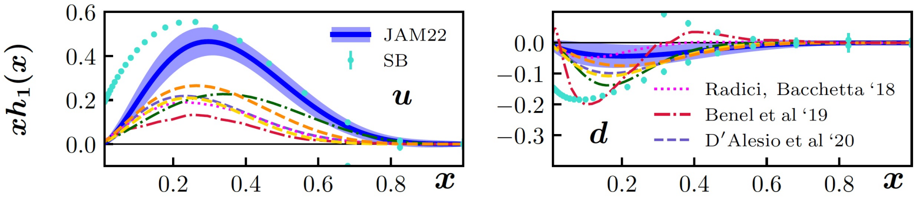

Fig. 2: Transversity PDF $xh_1^{u_v}$ (left) and $xh_1^{d_v}$ (right) plotted as a function of x at the scale $\mu^2 = 4\ \mathrm{GeV}^2$. The plot is from JAM3D-22 global analysis [12] (blue solid line with 1-σ error bars) and compares the results with alternate extractions from single hadron [13] (green dash-dotted line), [14] (yellow dashed line), [15] (orange dashed line), [16] (blue dashed line) and di-hadron [17] (magenta dotted line), [18] (red dash-dotted line) observables. The generated Soffer bound (SB) is also dusplayed (cyan points).

Note that, in order to suppress unwanted experimental effects, the experiments typically measure asymmetries like

$$A_{UT} = \frac{\Delta\sigma_{UT}}{2\sigma_{UU}} = \frac{\sigma_{UT}^{\uparrow} - \sigma_{UT}^{\downarrow}}{\sigma_{UT}^{\uparrow} + \sigma_{UT}^{\downarrow}}$$

where the superscripts indicating the target polarization state. In such asymmetries, also some theoretical contributions like gluon radiation and evolution effects tend to cancel out. Due to these reasons, the asymmetry observable is typically less sensitive to second-order corrections or to transitions in kinematical regimes. At the same time, asymmetries require knowledge of σ_{UU} to be solved in favor of the wanted ditributions. CLAS12 program will start with asymmetry measurements, but may be eventually extended to cross-section measurements as done by the precursor CLAS.

2.1 Transversity

The Transversity PDF h_1 describes the parton transverse polarization inside a transversely polarized nucleon, reflects the relativistic nature of parton confinement, and exhibits peculiar evolution properties. It is the least well known leading PDF that does not vanish when integrated in the parton transverse momentum $k_\perp$, and can thus be studied in the collinear limit. Because it is chirally-odd as associated to a flip of the parton helicity, it requires a peculiar fragmentation, also chirally-odd, to be observed in DIS reactions, see Sec 2.3.

The interpretation of single-hadron production

$$\sigma_{UT}^{Collins} \propto S_T\ \sin(\phi + \phi_S)\ C[h_1(x, k_T) \times H_1^{\perp}(z, p_T)]$$

requires the Collins fragmentation function $H_1^\perp$, and the TMD formalism to describe its genuine transverse-momentum dependence. Among the most recent extractions, some utilize only DIS data [19], some exploit DIS and e^+e^- data [13, 15, 16], some consider in addition inclusive single-spin asymmetries in proton-proton collisions [20, 12, 21]. Most of them impose the Soffer bound and some introduce constraints from Lattice calculations [19, 12].

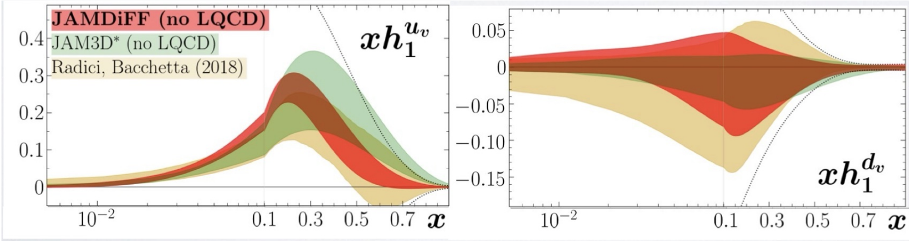

Fig. 3: Transversity PDF $xh_1^{u_v}$ (left) and $xh_1^{d_v}$ (right) plotted as a function of x at the scale $\mu^2 = 4$ GeV^2. The plot is from JAMDiFF analysis of di-hadron asymmetries [22] (red band) and compares the results with the alternate analysis [17] (yellow band) and the JAM3D single-hadron extraction [12] (green band). The Soffer bound is indicated by the dotted curve. A logaritmic scale is used below Bjorken $x = 0.1$.

The interpretation of di-hadron production

$$\sigma_{UT}^{IFF} \propto S_T \, \sin(\phi_{R\perp} + \phi_S) \sin(\theta) \; h_1(x) H_1^{\sphericalangle}(z, M_{hh})]$$

requires the interference fragmentation function $H_1^{\sphericalangle}$, and can be performed within the collinear formalism as it survives the $P_{h\perp}$ integration allowing to clear the convolution in transverse momentum. Here θ is the polar angle of the hadron production, $\phi_{R\perp}$ is the azimuthal angle of the *relative* momentum of the produced pair with mass M_{hh}. Among the most recent extractions, some utilize only SIDIS and e^+e^- data [18], some exploit also proton-proton collisions [17, 23, 22]. All analysis impose the Soffer bound and some introduce lattice constraints [23, 22].

Although essential for the description of nucleon structure, due to its chirally-odd nature, transversity has only recently been accessed in a limited kinematic range and with a large uncertainty [24]. A compendium of results is shown in Figure 2 and Figure 3. Recent phenomenological extractions typically peak in the region of $x \gtrsim 0.3$ where world data is very sparse. The dispersion of the extracted distributions manifests the uncertainty derived from the severe lack of data and the consequent model-dependent assumptions introduced as compensation.

The transversity first moment in Bjorken x, the tensor charge, is a fundamental quantity in quantum chromodynamics (QCD) connected to searches of beyond-the-Standard-Model phenomena such as the Electric Dipole Moment (EDM) of particles [29] and the tensor interaction [30]. From the above phenomenological analyses of the transversity function, constraints on the global g_T and flavor-separated δu, δd tensor charges can be inferred. Despite the large uncertainty, there is an apparent tension with the estimates derived from lattice

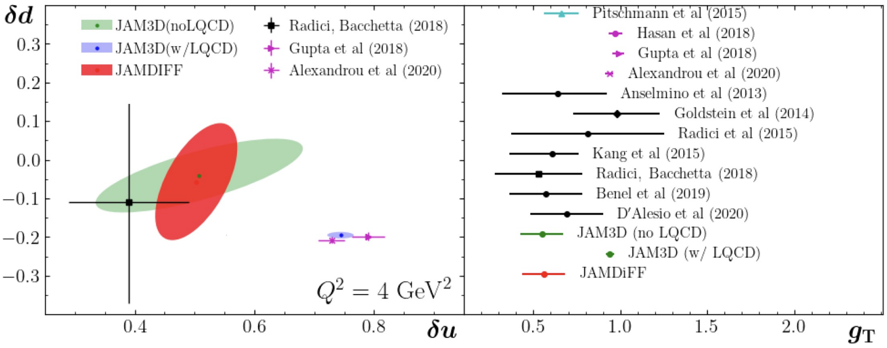

Fig. 4: The tensor charge δu, δd (left) and g_T (right) from [23]. Phenomenological extractions based on single-hadron observables [12] with (cyan) and without (green) inputs from lattice, and double-hadron observables [22] (red), are compared to previous extractions [17, 14, 25, 13, 18, 16], (black), are compared to lattice calculations [26, 27, 28] (magenta).

.

calculations, see Figure 4. Currently, the lattice constraints have a superior precision and, whenever introduced in the phenomenology extractions, as done in [20, 23, 22], completely dominate the result. This signals a lack of competitive experimental data sets.

The CLAS12 data from RGH will cover an unexplored kinematic regime at high Bjorken-x (valence region) and will allow multi-dimensional analyses over all the relevant kinematical dependencies. The tensor charge receives substantial contributions in the valence-quark region at $x \gtrsim 0.3$. While this is true for many polarization-dependent PDFs, this feature is even stronger for transversity as the contribution from gluons is vanishing due to its chirally-odd nature. New data in the uncharted valence-quark region can clarify the current tensions between extractions from phenomenology and lattice. The proposed run group will provide unprecedented constraints to the tensor charge and allow a precise comparison with lattice QCD, see Sec. 6.1.

2.2 Sivers

The **Sivers** PDF $f_{1T}^{\perp}$ is a genuine TMD function which vanishes with $k_\perp$ integration. Among the most intriguing parton distributions, it requires a non-zero parton orbital angular momentum and a correlation with the nucleon spin. As a consequence of its non-trivial gauge-invariant definition, the Sivers function probes QCD at the amplitude level: it is naively T-odd (do not violate T-invariance due to the interaction phase) and exhibits a peculiar process dependence. A sign change is expected when moving from SIDIS to Drell-Yan processes, whose verification is one of the most urgent goals of the present experimental activity [24]. It is among the few TMDs that, while describing the non-perturbative nature when $k_\perp \ll Q^2$, should in principle match the perturbative regime with increasing transverse momentum, providing a formal bridge between the two QCD descriptions [31]. It can be studied in single-hadron production as transversity, but with a different azimuthal modulation and in conjunction with the ordinary unpolarized fragmentation function:

$$\sigma_{UT}^{Sivers} \propto S_T \, \sin(\phi - \phi_S) \; C[f_{1T}^{\perp}(x, k_T) \times D_1(z, p_T)]$$

CLAS12 data will allow an extended coverage in the valence region and a disentaglement of the Sivers kinematic dependences, a crucial information for the study of these phenomena and the connections among different QCD regimes.

2.3 Collins and Interference Fragmentation

The **Collins** and **Di-hadron** FFs originate from spin-orbit effects connecting the spin of a fragmenting quark with the final observed hadron or dihadron transverse momentum, respectively. Convincing evidences have been found for the existence of these mechanisms [24]. These peculiar FFs act as a quark polarimeter and allow one to access the elusive chirally-odd distribution functions in SIDIS reactions. In particular the Collins FF features a real dependence in transverse-momentum (does not survive a p_T intergration) and requires a genuine TMD formalism. In contrast, the Interference FF sensitive to the hadron pair *relative* transverse momentum can be studied in the collinear limit, providing a complementary access to transversity that does not depend on the TMD formalism, and can be reliably extended to the hadron-hadron scattering case [17]. High-precision data from CLAS12 can complement present and future information gathered at the much higher center-of-mass energy of experiments at the e^+e^- colliders [32], like BELLE-II, and at hadron-hadron colliders, like PHENIX and STAR [33].

2.4 DVCS on transversely polarized proton and the GPD E

The formalism of GPDs [34, 35, 36, 37, 38, 39, 40] provides a universal description of the partonic structure of the nucleon, providing the spatial distributions in the transverse plane of partons carrying a given longitudinal momentum fraction. The simultaneous knowledge of longitudinal momentum and transverse position gives access to the angular momentum of quarks and gluons. Therefore, the determination of GPDs can clarify the so-called “spin crisis”, which ensued from the measurements showing that the spins of the quarks contribute to only 20-30% of the nucleon’s spin. GPDs are most easily accessed in the measurement of the exclusive leptoproduction of a photon (DVCS, which stands for Deeply Virtual Compton Scattering) on the nucleon, at sufficiently large Q^2, which is the virtuality of the photon emitted by the initial lepton ($Q^2 = -(k - k')^2$, where k and k' are the momenta of the initial and final state leptons, respectively). Figure 5 illustrates the leading-order diagram for DVCS, where QCD factorization is applied, splitting the process into the hard quark-photon scattering part, calculable in perturbative QED, and the soft nucleon-structure part. Considering only helicity-conserving processes and the quark sector, the soft structure of the nucleon is parametrized by four GPDs for each quark flavor: $H, \tilde{H}, E, \tilde{E}$ (the tilde denotes polarized GPDs), which depend, in leading-order and leading-twist QCD, upon three variables: x, ξ, and t. x, the average parton momentum fraction, is not accessible experimentally in the DVCS process. $x+\xi$ and $x-\xi$ are the longitudinal momentum fractions of the quarks, respectively, coming out from and going back into the nucleon. t is the squared four-momentum transfer between the final and initial state nucleons.

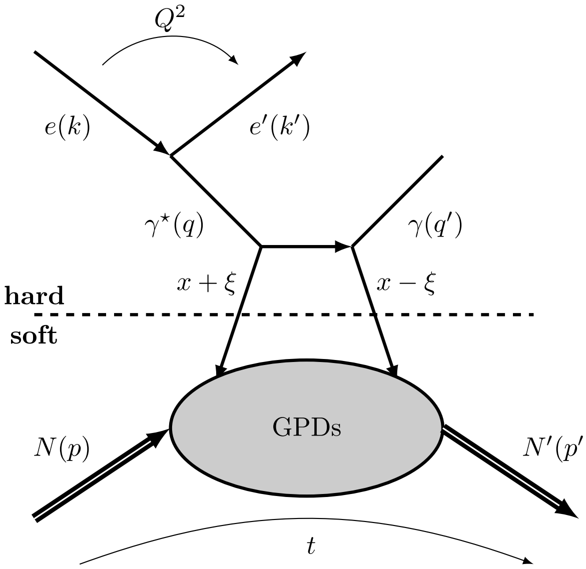

Fig. 5: The "handbag" diagram for the DVCS process on the nucleon $eN \to e'N'\gamma$. The four-vectors of the incoming/outgoing electrons, photons, and nucleons are denoted by k/k', q/q', and p/p', respectively. $t = (p-p')^2$ and ξ is proportional to the Bjorken variable x_B ($\xi \simeq \frac{x_B}{2-x_B}$, where $x_B = \frac{Q^2}{2M\nu}$, M is the nucleon mass, and $\nu = E_e - E_{e'}$).

DVCS shares the same final state with the Bethe-Heitler (BH) process, where a real photon is emitted by either the incoming or the scattered electron. At the cross-section level BH is typically larger than DVCS, but information on the latter can be obtained by extracting the DVCS/BH interference term, and exploiting the fact that the amplitude from BH can be computed. Spin-dependent asymmetries, which at leading-twist depend mainly on the interference term, can then be connected to linear combinations of real and imaginary parts of Compton Form Factors (CFFs, $\mathcal{F} = \{\mathcal{H}, \mathcal{E}, \tilde{\mathcal{H}}, \tilde{\mathcal{E}}\}$), defined for a generic GPD F ($F = \{H, E, \tilde{H}, \tilde{E}\}$) as

$$\Re\mathrm{e}\mathcal{F} = \mathcal{P}\int_0^1 dx \left[\frac{1}{x-\xi} \pm \frac{1}{x+\xi}\right] [F(x,\xi,t) \mp F(-x,\xi,t)] \tag{1}$$

$$\Im\mathrm{m}\mathcal{F} = F(\xi,\xi,t) \mp F(-\xi,\xi,t), \tag{2}$$

where $\mathcal{P}$ is the principal value of the integral, and the top and bottom signs apply, respectively, to the unpolarized GPDs (H, E) and to the polarized GPDs ($\tilde{H}$, $\tilde{E}$).

Measuring GPDs is a complex task, calling for a long-term experimental program comprising the measurement of different observables [41, 40]. Such a dedicated experimental program, mainly focused on a proton target, has been carried out worldwide, in particular at JLab, with CLAS/CLAS12 and Hall A [42, 43, 44, 45, 46, 47, 48, 49, 50], at HERA with HERMES [51, 52, 53, 54, 55, 56, 57], H1 [58, 59, 60], and Zeus [61, 62] and at CERN with COMPASS [63], bringing strong constraints to the GPD H and indications on the size and kinematic dependence of $\tilde{H}$.

Measuring DVCS on transversely polarized protons is essential to quantify the quarks' angular momentum contribution to the proton's spin. Indeed, the transverse-target spin asymmetry (TTSA, hereafter also denoted by A_{UT} where T indicates the transversely polarized target and U the unpolarized beam) for DVCS on the proton is strongly sensitive to the GPD E, which is poorly known and constrained. E is of particular interest as it enters, along with H, in Ji's sum rule [35]

$$\sum_q \int_{-1}^{+1} dx\, x[H^q(x,\xi,t=0) + E^q(x,\xi,t=0)] = 2\, J_q, \tag{3}$$

which links the total angular momentum J_q carried by each quark q to the sum of the second moments over x of the GPDs H and E.

All terms contributing to the exclusive photon leptoproduction cross section have been expanded by Belitsky, Mueller, and Kirchner [64] up to twist-3 in Fourier series in ϕ. In the case of a transversely polarized target the expansion is done also as a function of $\phi - \phi_S$, where ϕ_S, the angle between the lepton scattering plane and $S_\perp$, the component of the target polarization vector that is orthogonal to $\vec{q}$ (Fig. 6).

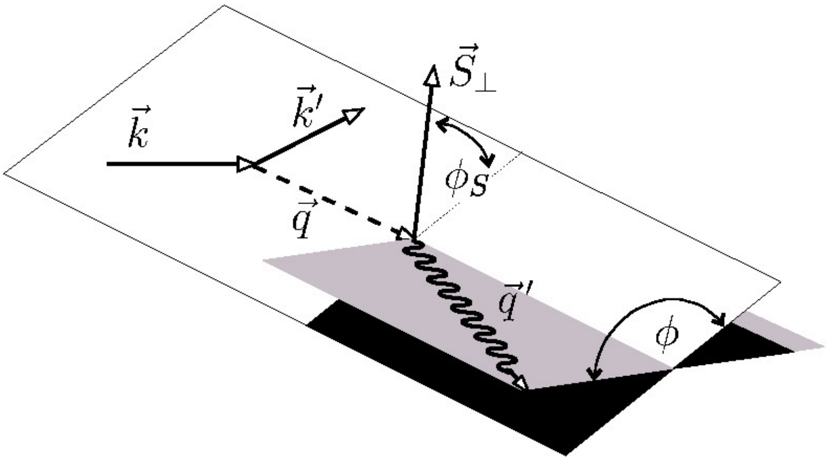

Fig. 6: Scheme illustrating the definition of the angles ϕ, formed by the leptonic and hadronic planes, and ϕ_S formed by the lepton scattering plane and $S_\perp$, the component of the target polarization vector that is orthogonal to $\vec{q}$.

.

The contribution to the total cross section coming from the BH-DVCS interference is given, in the case of a transversely polarized target, by:

$$
\begin{aligned}
d\sigma^{\mathrm{I}}_{UT} &= \frac{-K_{\mathrm{I}}}{\mathcal{P}_1(\phi)\mathcal{P}_2(\phi)} \left\{ \sum_{n=0}^{3} c^{\mathrm{I}}_{n,\mathrm{TP}-} \sin(\phi-\phi_S)\cos(n\phi) + \right. \\
&\left. \sum_{n=1}^{3} s^{\mathrm{I}}_{n,\mathrm{TP}+} \cos(\phi-\phi_S)\sin(n\phi) \right\},
\end{aligned}
\tag{4}
$$

(5)

The extraction of A^{I}_{UT} gives an access to the leading Fourier coefficient in 4, which, in turn, relates to the CFF as

$$
\begin{aligned}
c^{\mathrm{I}}_{1,\mathrm{TP}-} &\propto -\frac{M}{Q}\Im\mathrm{m}\left\{ \frac{t}{4M^2}\left[(2-x_B)F_1\mathcal{E} - 4\frac{1-x_B}{2-x_B}F_2\mathcal{H}\right] \right. \\
&+ \left. x_B\xi\left[F_1(\mathcal{H}+\mathcal{E}) - (F_1+F_2)(\tilde{\mathcal{H}} + \frac{t}{4M^2}\tilde{\mathcal{E}})\right]\right\},
\end{aligned}
\tag{6}
$$

where F_1 and F_2 are the Dirac and Pauli form factors. Therefore, the measurement of A_{UT} with a proton target provides a rare access to the CFF $\Im\mathrm{m}\mathcal{E}$ with no kinematic suppression of its contribution relative to those of the other CFFs.

2.5 Correlators

Lattice has made remarkable progress in the recent decades [65].

It is worth mentioning that, besides the selected fundamental measurements discussed above, many other important observables can be measured simultaneously with a transversely polarized target. In practice, in fact, azimuthal amplitudes sensitive to the poorly known leading-twist “pretzelosity” $h_{1T}^{\perp}$ and “worm-gear” g_{1T} TMDs, as well as to several sub-leadings-twist transverse-momentum-dependent PDFs and FFs [66, 24] can be extracted simultaneously in the analysis of the same data. Furthermore, the poorly known transversity (chiral-odd) GPDs H_T and $\tilde{H}_T$ can be accessed in deeply virtual pseudo-scalar meson production (DVMP) with a transversely polarized target [67, 68].

2.6 Competition

Since the last jeopardy review in 2020, few new results became available on the electro-production of mesons off a transversely polarized target. COMPASS published the study on dihadron transverse-spin-dependent asymmetry on proton and deuterium targets [69], and the results on the deuteron data from 2022 run [70]. HERMES completed a multi-dimensional fit [71] and COMPASS a P_T-weighted analysis [72] of already published data. All these results are limited to Bjorken x below 0.3. COMPASS published preliminary Drell-Yan data consistent with the fundamental QCD prediction of a sign change of naive time-reversal-odd TMD PDFs (i.e. Sivers) when comparing the Drell-Yan process

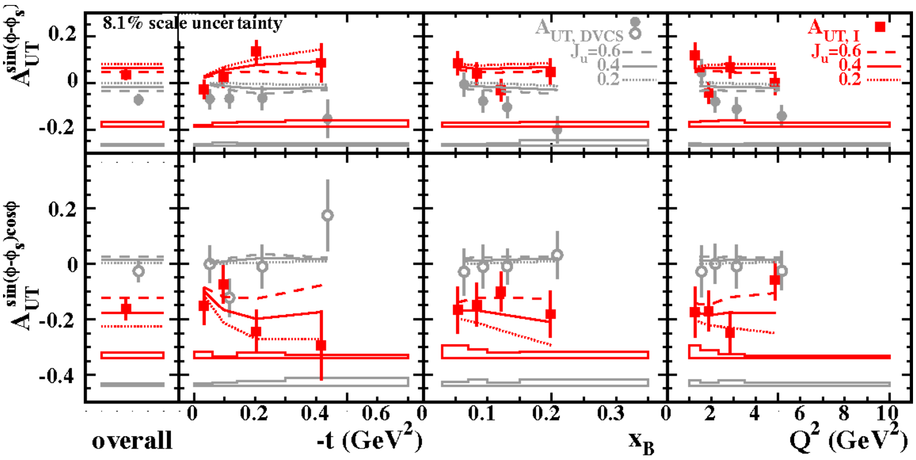

Fig. 7: Asymmetry amplitudes of the squared DVCS amplitude $A_{UT,DVCS}$ (circles) and the interference term $A_{UT,I}$ (squares). The error bars (bands) represent the statistical (systematic) uncertainties, excluding the 8.1% scale uncertainty due to the target polarization measurement uncertainty. The curves are predictions of the VGG model [**?**, **?**, **?**, **?**], with three different values for the u-quark total angular momentum J_u and fixed d-quark total angular momentum $J_d = 0$ [**?**]. The figure is from Ref. [**?**].

with SIDIS [73]. The interest in data on transversely polarized targets is manifest from the steady flow of phenomenological analyses of the sparse SIDIS data collected in the past couple of decades, in conjunction with proton-proton, e^+e^- and Drell-Yan data [23, 21].

No new DVCS results on transversely polarized targets became available after the low-statistics, limited-coverage HERMES data were released, and the RGH experiment provides the only chance to overcome this lack of information. The DVCS results from HERMES [53] are presented on Fig. 7, in the entire kinematics range ($< -t >= 0.12$ GeV^2, $x_B = 0.09$, $< Q^2 >= 2.5$ GeV^2). The amplitudes $A_{UT,\mathrm{DVCS}}$ and $A_{UT,\mathrm{I}}$ for the same azimuthal dependence are shown together in each panel. The filled symbols represent the asymmetry amplitudes related to different coefficients of the BMK expansion. The amplitudes represented by the unfilled symbols are expected to be suppressed, and are indeed found to be typically small. The amplitudes $A_{UT,\mathrm{I}}^{\sin(\phi-\phi_S)\cos(n\phi)}, n = 0, 1$ were found to have substantial magnitudes with opposite signs but with little kinematic dependence. The overall result of the amplitude $A_{UT,\mathrm{DVCS}}^{\sin(\phi-\phi_S)}$, shown in the top row of Fig. 7, is non-zero by 2.8 times the total uncertainty. The amplitude $A_{UT,\mathrm{DVCS}}^{\sin(\phi-\phi_S)\cos\phi}$, expected to be suppressed, was indeed found to be small.

Therefore, the HERMES data present kinematic dependencies of moments of A_{UT} on one variable at a time, integrating on the others. The RGH data will instead allow a first-time extraction of the full ϕ dependence of the DVCS TTSA in 4-dimensional bins (Q^2, x_B, $-t$, ϕ), and will cover a much wider phase space than the one spanned by HERMES. This will be presented in detail in Sec. 6.

Lattice calculations are making steadily progresses [74, 75] and can offer benchmark quantities or complementary constraints to the phenomenological models.

The SoLID experiment [76, 77] has been mentioned as a strategic opportunity in the 2023 Long Range Plan for Nuclear Science and is awaiting CD0. New channels of investigation are being explored [78, 79] and phenomenological studies are awaiting new inputs [80, 81].

3 Experimental Details

The RGH experiment exploits the CEBAF high quality beam [82] in conjunction with the large acceptance CLAS12 spectrometer [83] in Hall B, complemented by a transversely polarized target (see Sec. 4.1) and a dedicated recoil detector (see Sec. 4.3).

3.1 CLAS12 Spectrometer

The CLAS12 spectrometer has been designed to run at high luminosity, up to about 3 orders of magnitude higher than the precursor experiments like HERMES and COMPASS, and bring the 3D nucleon structure studies into the precision phase. CLAS12 started the data taking with unpolarized hydrogen targets in spring 2018 and has been running successfully since, with different targets and detector configurations. In particular, CLAS12 successfully ran with longitudinally polarized NH_3 and ND_3 targets in 2022-2023. Detailed calibration procedures and event reconstruction algorithms have been developed to reach a performance close to, or in some cases superior of, the design specifications.

3.1.1 Forward Detector

With respect to the goals of run-group H, the CLAS12 spectrometer has specifically demonstrated to be able to achieve the following performances:

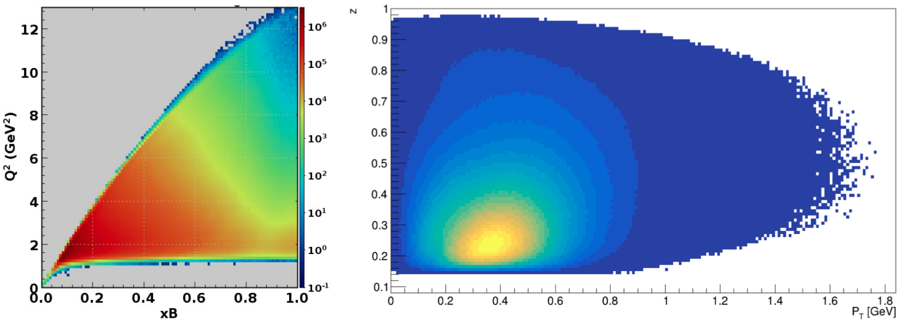

Fig. 8: The CLAS12 reach in the relevant kinematic variables at a beam energy of 10.6 GeV. (Left) Inclusive electron coverage in the hard scale Q^2 versus Bjorken x. (Right) Charged hadrons coverage in the transverse momentum P_T versus the fractional energy z.

Tracking The single-track forward reconstruction efficiency has been improved with the implementation of Machine-Learning algorithms to support effective denoising and track segment finding, to a level of better than 90% at the design luminosity of 1×10^{35} cm^{-2}s^{-1}, with a dependence on the beam current of $98 - 0.1 \times \mathrm{I}\,(\mathrm{nA})$ percent. The typical measured resolutions in the relevant kinematic quantities are $\sigma_p/p = (0.5 - 1.5)\%$ and $\sigma_\theta = 1 - 2$ mrad [83].

Scattered Electron The efficiency of the CLAS12 trigger for DIS events, with the electron scattered inside the acceptance at an energy above 1.5 GeV, is greater than 99% [84]. Electrons are identified by a combination of signals in the Cherenkov counters and calorimeters. Thanks to the large acceptance of CLAS12, scattered electrons are detected in a wide kinematic range from elastic events to DIS, with an extended reach at large values of Q^2, Bjorken x, and forward hadron kinematics (see Fig. 8).

Exclusive events Event selection and background suppression has been successfully achieved in the CLAS12 environment. The large amount and variety of collected data and the gained experience provide a solid ground for any new development. The DVCS final state in the $ep\gamma$ topology has been successfully extracted from the NH_3 and ND_3 data of Run Group C, taken with the longitudinally polarized target (two analyses are in the final stages). An interesting study is ongoing to exploit Machine-Learning techniques for the identification of exclusive DVCS events based on the electron and photon information provided by the CLAS12 Forward Detector with no (or partial) recoil proton information. Promising results have been obtained on RGA data, with increased statistics and comparable physics observable with respect to the traditional analysis based on a complete recoil reconstruction. In the case of RGH, such a technique can provide a systematic check for the standard DVCS analysis in the $ep\gamma$ topology, and extend its kinematical coverage beyond the acceptance of the recoil detector.

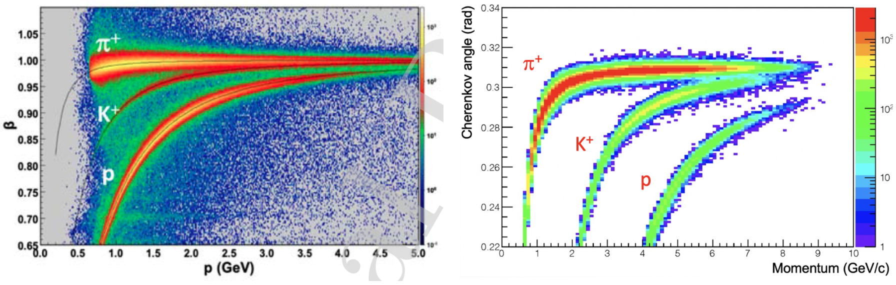

Fig. 9: (Left) The hadron separation provided by the Forward Time-Of-Flight system. (Right) The hadron separation obtained by the RICH detector.

Hadron PID Identification of hadrons is essential to gather flavor information in SIDIS observables. The CLAS12 Forward Time-Of-Flight system (FTOF) provides an excellent pion separation from kaons and protons at momenta up to about 3 GeV/c and 5 GeV/c [85], respectively, see left panel of Fig. 9. To complement the CLAS12 baseline configuration and provide hadron separation in the whole range of interest for SIDIS physics, up to momenta of 8 GeV/c, a ring-imaging Cherenkov detector (RICH) has been realized. The first module was installed in 2018 before the start of CLAS12 data taking and the second module completed in 2022 before the start of the RGC polarized target run [86]. Data analysis shows that the CLAS12 RICH is able to achieve a time resolution of ≈ 0.7 ns and a Cherenkov angle resolution of ≈ 1.5 mrad [87], matching specifications, and provide hadron separation in the wanted momentum range, see right panel of Fig. 9.

3.2 Beamline Elements

The standard beamline equipment in Hall B comprises position, current, and halo monitors, connected to the interlock system. Among the Beam Position Monitors (BPMs), three nA BPMs, (2C21 at the beginning of the tunnel, 2C24 at the end of the tunnel before the hall proper, and 2H01 on the space frame), measure beam transfer (x,y) position relative to their center as well as the beam current. The stripline BPMs (2H00 close to the target and other on the upstream tunnel) measure the beam position but are reliable only for beam currents above 25 nA and will not be used by RGH. The position monitor 2H01 (together with 2H00 if the current is high enough) close to the interaction region is the most important one to keep the beam position steady on the target. A feedback system (the orbit locks) uses (x,y) positions on this BPM, and the Horizontal and Vertical correctors on 2C22/2C23/2H00 girders to keep the beam position stable.

The Hall-B Faraday cup provides an instantaneous beam current reading. It is not cooled and cannot operate at high currents but works fine at 1 nA, with an integrated rate of 906.2 counts/sec. The Synchrotron Light Monitor (SLM) measures the amount of synchrotron light generated by the electron beam in the magnetic field of the last dipole right before the Hall-B upstream tunnel. The main use of this current monitor is to measure the helicity-related beam intensity (charge) asymmetry but can be used for beam-charge accounting if needed.

The beam-halo counters consist of photomultiplier tubes with plastic attached to their photocathodes strapped to the beam pipes along the beamline. The rates in halo counters are good indicators of the beam transport quality. In addition to the halo counters, there is a beam offset monitor (BOM) just upstream of the target.

The CLAS12 beamline has already operated at a beam current of 1 nA. Some specific monitors cannot work at such a low beam current, but there is enough redundancy in current and position monitors to ensure a normal operation and safe control. The same beam raster utilized for the RG-C operation will be used (note that the target material is the same), with a radius envelope of 6.5 mm and a frequency of 1 Hz.

4 Required Equipment

4.1 Transverse Target

The experiments described here will utilize a new, dynamic nuclear polarized (DNP) target of solid ammonia (NH_3), specifically designed to operate inside the CLAS12 High Threshold Cherenkov Counters (HTCC). The ammonia samples will be continuously polarized using microwave-induced spin-flip transitions at a temperature of 1 K and in a 5 T magnetic field. Similar target systems have been used with success at JLab in experimental halls A, B, and C [88, 89, 90] and with electron beam currents up to 140 nA. Most recently, a longitudinally polarized target of NH_3 and ND_3 was used for the Run Group C experiments with CLAS12 [91]. In this system, the 5 T polarizing field was provided by the CLAS12 solenoid, which will be removed for Run Group H in order to install a 5 T split-coil magnet with a vertical field orientation. While the magnetic field

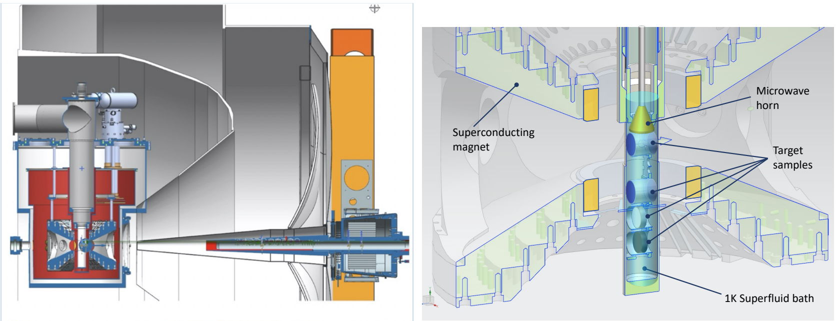

Fig. 10: Left: Conceptual design showing the dynamically polarized target at the center of the CLAS12 HTCC. Right: Closeup of target samples suspended in superfluid helium.

requirements for frozen-spin polarized targets are less stringent, beam heating and radiation damage exclude their use in the CEBAF electron beam [92]. One advantage of DNP is that the target's polarization direction can be made parallel or anti-parallel to the applied field by a slight adjustment of the microwave frequency. Reversing the polarization typically requires less than four hours.

The target considered here will resemble a compact version of the system used in Hall C and Hall A and most recently described by Pierce *et al.* [88]. A vertical ladder suspends multiple target cells into a pumped bath of superfluid helium at 1 K (Fig. 10). For the RGH experiments, the ladder will have two cells $(\varnothing 1.5 \times 2.0)$ cm^3 filled with 1–2 mm granules of frozen ammonia (0.87 g/cm^3), an empty cell, as well as carbon and polyethylene (CH_2) samples for background and dilution studies. As has been the case in the Hall A and C polarized targets, small NMR coils will be located inside the ammonia cells for measuring the proton polarization with a relative accuracy of about 4%. The coils are fabricated from 1 mm capillary surrounded by a teflon sleeve, and reduce the filling factor of the cells by a few percent. The cells are machined from PCTFE, a fluorinated plastic that is transparent to the 140 GHz microwaves for polarizing the ammonia but does not produce a background proton NMR signal. Thin aluminum windows are glued to their upstream and downstream faces. The superfluid bath is constrained by a thin-walled aluminum tube. The superfluid and aluminum windows contribute to the overall scattering at the level of about 25% (Table 1).

Liquid helium to the target will be supplied by the Hall B buffer dewar and pumped to a vapor pressure of approximately 0.1 torr by a set of high-capacity Roots pumps. Each target cell will contain about 2 g of solid ammonia and will require less than 0.5 W of microwave power for optimum polarization. Heat from the 1 nA beam will deposit less than 10 mW.

The 5 T superconducting magnet will be similar in design to the split-coil magnet intended for transversely polarized target experiments in Hall C. Unfortunately, this magnet was designed for a horizontal field orientation and cannot provide the 60° aperture for scattered protons that is needed for the DVCS portion of this proposal. The superconducting windings of the new magnet will be identical to the existing magnet but will be separated by an aluminum frame with a more favorable geometry for RGH. The magnet and 1 K refrigerator will

Item	Number	Material	Density g/cm^3	Length cm	Thickness g/cm^2
Bath windows	2	AL7075	2.81	0.01	0.056
Superfluid	2	He-II	0.14	0.2	0.058
Cell Windows	2	AL6061	2.70	0.003	0.016
Ammonia	1	NH_3	0.52	2.00	1.04
Superfluid	1	He-II	0.06	2.00	0.12

Tab. 1: Materials in the beam around the polarized target. The first superfluid entry corresponds to liquid helium outside the target cell, and the second to liquid inside the cell. The density of materials inside the cell have been adjusted for an ammonia packing fraction of 0.6.

be housed in a vacuum chamber with a thin aluminum exit window matching the aperture of the magnet (Fig. 36).

Based on previous experience at JLab, proton polarizations of 90% or higher can be expected. Radiation damage from the electron beam slowly destroys the polarization, and so the beam will be rastered over the face the target to reduce this effect. After a dose of about 2.5×10^{15} e^{-1}cm^{-2}, the damage can be partially repaired by annealing the sample to about 90 K for several minutes (Fig. 12). Assuming a beam current of 1 nA and a raster diameter of 1.3 cm, an ammonia sample can last approximately six days before annealing is necessary. With two ammonia samples on the ladder, anneals will take place after about 14 days of beam. This process can be performed *in situ* and remotely, using heaters inside the target cryostat, and will require about 4 h with polarization recovery.

However, the annealing procedure becomes progressively less successful, and the ammonia must be replaced after about five or six anneals. With two ammonia samples on the ladder, this corresponds to about 70–80 days of beam before the ladder must be replaced.

Due to a lack of overhead space, the target cryostat must be removed from the HTCC in order to remove and replace the target ladder. For this purpose it will be attached to a cart mounted on the Hall B rail system, as has been the case with nearly all target systems utilized with both CLAS and CLAS12, including polarized targets. The cryostat only needs to be retracted about 60 cm in order to access and remove the sample ladder, but this could require significant disassembly of some beamline components. We make the conservative estimate that up to 48 h will be needed to perform this operation, and it will be performed twice.

The target polarization will be measured using the standard method of continuous-wave NMR, in which the polarization is proportional to the area under the NMR absorption signal (Fig. 13). The constant of proportionality is determined by measuring the signal using a sample of known polarization. This is achieved by allowing the sample spins to come into thermodynamic equilibrium with the superfluid bath, in which case the polarization is given by Maxwell-Boltzmann statistics as $\tanh(\mu_p B/kT)$, where μ_p, B, k, and T are the proton magnetic dipole moment, the field strength, Boltzmann constant, and bath temperature, respectively. These “thermal equilibrium” (TE) calibrations should be performed routinely to reduce the systematic error of target polar-

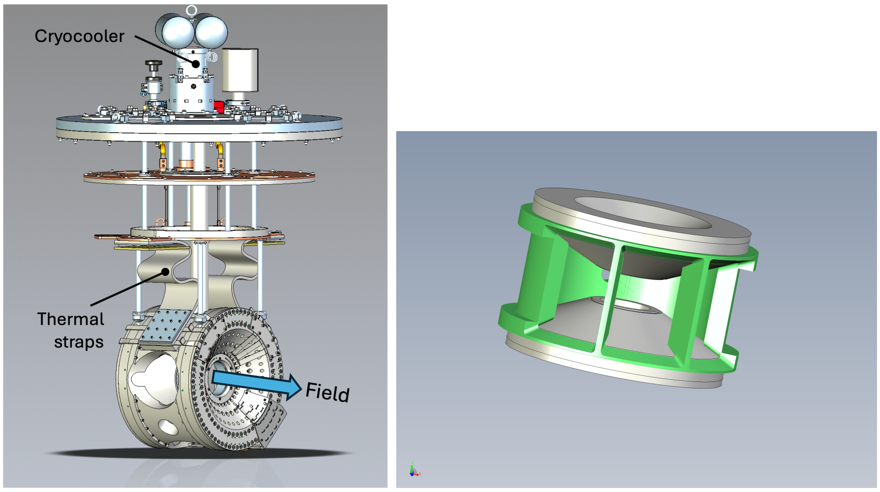

Fig. 11: Left: Superconducting magnet for polarized target experiments in Hall C. The magnet has been successfully tested to 5 T at Jefferson Lab. Right: Conceptual redesign of the magnet coils with a different intercoil support (green) for RGH. The opening in the forward directions for scattered particles spans ±60° in the horizontal plane and ±25° in the vertical. The magnet is rotated to produce a vertical field.

ization. Because the proton's TE polarization is quite small (0.5% at 5 T and 1 K), significant signal averaging is needed for an accurate measurement. We envision making the calibrations once per week, requiring eight hours.

We calculate the overhead associated with these target operations over the course of a 120 day (17 week) experiment with the assumptions listed below and find a total of about nine days. We anticipate that the overhead can be reduced by coordinating these operations with scheduled CEBAF beam study and maintenance periods.

- TE calibrations (with polarization recovery) will be performed every week, requiring eight hours. Total number: 17. Total time: 136 h
- Anneals (with polarization recovery) will be performed once every two weeks, requiring four hours. Total number: 8. Total time: 32 h.
- The target ladder will be replaced two times, requiring 24 hours. Total time: 48 h.
- Total overhead: 216 h (9 days)

An idealized two-week (42 shift) operational sequence that is based on these estimates is given below. In this scenario, background measurements constitute about 15% of the beam time. Polarization loss due to radiation damage is partly compensated by spending less time with the initial target polarity and reversing the order of the polarity for the second ammonia target.

- 8 shifts, + polarity with Ammonia target #1;
- 9 shifts, - polarity with Ammonia target #1;

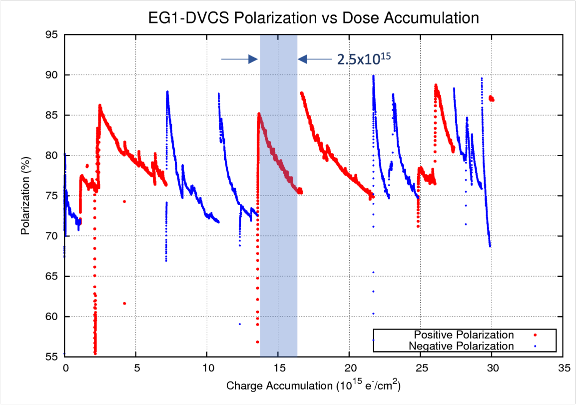

Fig. 12: Performance of the 6 GeV CLAS polarized target during the EG1-DVCS experiment. The shaded band indicates a depolarizing dose of 2.5×10^{15} $\mathrm{e}^{-1}\mathrm{cm}^{-2}$.

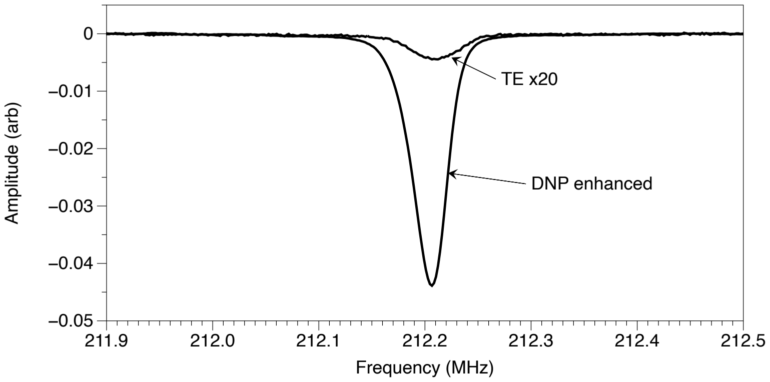

Fig. 13: NMR signals for protons in thermal equilibrium (TE) at 1 K and enhanced by DNP to approximately 90%. The TE signal is multiplied by twenty for clarity.

- 3 shifts, background studies (C, CH_2 or empty);
- 1 shifts, TE calibration;
- 8 shifts, - polarity with Ammonia target #2;
- 9 shifts, + polarity with Ammonia target #2;
- 2.5 shifts, background studies (C, CH_2 or empty);
- 1.5 shifts, Anneal + TE calibration;

4.2 Beam Chicane

The 5 T polarizing field of the target is transverse to the beam. Its integral of 1.64 Tm implies a deflection of 2.15 degree for 10.6 GeV beam particles. A

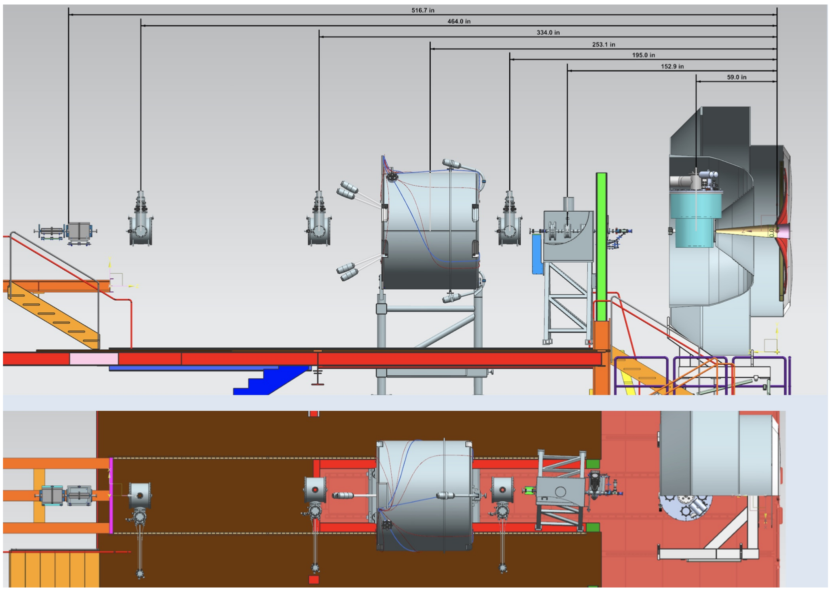

Fig. 14: (Left) The magnet chicane to compensate the beam bending of the target holding magnet (left). The 5.0 T split-pair magnet from Cryo-Magnets Inc. (right).

magnet chicane has been designed in order to compensate such a bending and ensure that the non-interacting particles pass by the experiment, and reach the Hall-B dump within the downstream vacuum pipe, without further interactions.

The chicane needs to be compact to fit within the constrained space of the Hall-B beamline. A workable solution has been outlined that is compatible with the other beam elements and the CLAS12 solenoid, when the latter is moved into a park position, see Figure 14. It can be realized with commercially available superconducting 7.5 T split-pair magnets, e.g from CryoMagnets Inc. [93]. With respect to items in stock, minor modifications are required: a change of orientation of the cooling head and a widening of the cryostat bore in the bending plane. The field uniformity is sufficient to avoid beam orbit perturbations even accounting for a rastered beam with a radius envelope of 7 mm, see Section 3.2.

The beam chicane generates synchrotron radiation upstream of the detector. According to analytic estimates and past experience, no real issue was anticipated. Nevertheless, a dedicated study has been pursued with GEANT simulation. The chicane model has been implemented in the GEMC framework used by CLAS12, see Figure 15. The field of the chicane magnets has been rescaled (down) to match the same field integral of the target magnet. The central magnets have been moved off axis by 13 cm to align with the bended beam. Simulations show that beam particles are transported through the chicane along the expected trajectory, impinge on the target at the desired angle, and align downstream to the axis of the CLAS12 vacuum pipe, see Figure 16. The photons are generated in the bending sections of the line (where a significant magnetic field is present) and span an horizontal flare that could extend into CLAS12 in absence of any material. The beam pipe itself, plus 15 mm lead shield in the relevant positions, are enough to effectively suppress the synchroton photons generated upstream. The vast majority of the synchroton radiation generated close to the interaction region is trapped inside the downstream CLAS12 vacuum pipe. The 1% surviving fraction escapes the vacuum pipe due to rescattering. This amounts to an O(1 GHz) photon flux distributed over the entire multi squared-meter surface of the CLAS12 Forward Detector, see Figure 17. Simulations show that this flux does not generate any significant background in the experiment, as expected by its low-energy spectrum peaked at 0.1 MeV.

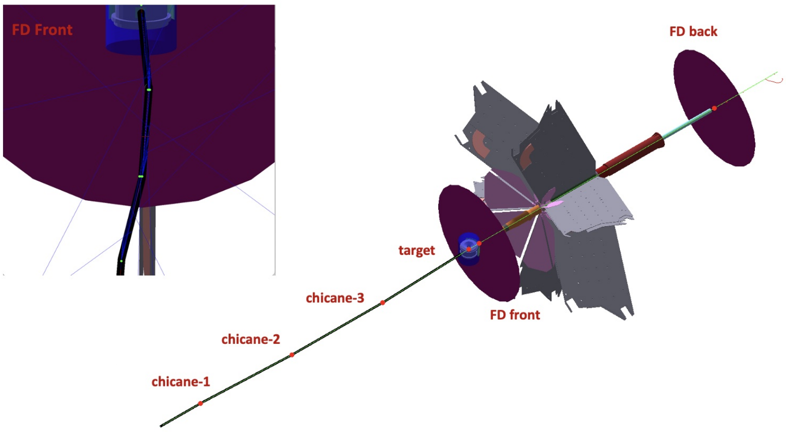

Fig. 15: The magnet chicane implemented in the CLAS12 GEMC simulation framework. The passing particles are recorded by flux planes at the magnet locations, and on the front and back faces of the CLAS12 Forward Detector (only the torus magnet structure is visible for simplicity). The insert shows a section of the beam pipe, with the synchroton photon trajectories shown in blue.

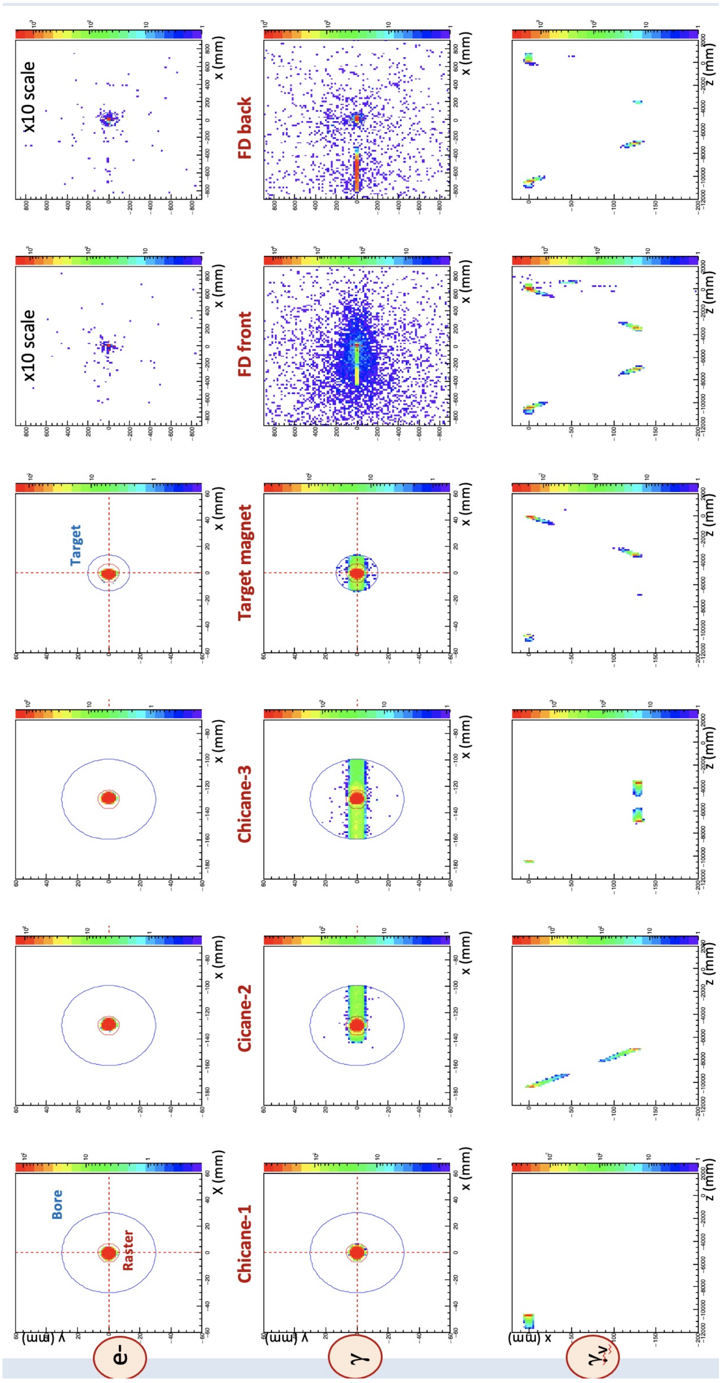

Fig. 16: First and second row: spatial distribution of the beam particles on relevant planes along the CLAS12 beamline. Along the row: center of the first, second and third chicane magnet, center of the target magnet, front and back face of the CLAS12 Forward Detector. Third row: emission point of the synchrotron photons impinging on the same planes above. The electron beam particles are transported through the chicane along the expected trajectory (first row). The synchrotron photons create a horizontal flare (second row) because emitted (at a varying angle) in the bending sections of the beam line (third row). The beam pipe and shielding have been removed to allow free flight of particles.

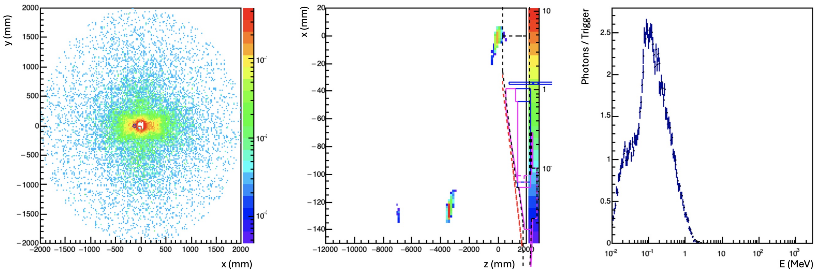

Fig. 17: Spatial distribution at the front of the CLAS12 Forward Detector (left), emission vertex position (center) and energy spectrum (right) of the synchrotron photons escaping the beam pipe and a 15-mm lead shielding. The last panel is normalized to the number of triggers, i.e. data acquisitions with a gate of 252 ns at the RGH luminosity.

4.3 Recoil Detector

The chosen target magnet structure provides open acceptance in the angular region favored for recoil detection, up to 70 degrees (and beyond, thanks to the magnet bending). Protons below 30 degrees are anyway detected in the CLAS12 Forward Detector. In order to detect protons at larger angles, a dedicated recoil detector will be implemented exploiting the left and right openings in the magnet structure. In each side, a simple geometry based on four detection planes, three tracking and one time-of-flight (TOF) plane, is anticipated. The solid angle coverage should match the magnet apertures and span ± 25 degrees vertically and 29 degrees horizontally, leaving a blind central region of ± 40 degrees. The distance from the center of the target is chosen to optimize acceptance within the clearance of the CLAS12 HTCC (see Table 2).

Plane	Name	Distance from IP (mm)	Width (mm)	Height (mm)
1	Tracker Region 1	440	227	410
2	Tracker Region 2	720	372	671
3	Tracker Region 3	1000	517	933
4	Time-of-flight	1220	650	1160

Tab. 2: Dimensions of the RGH recoil detector planes covering the magnet apertures on the left and right side of the target.

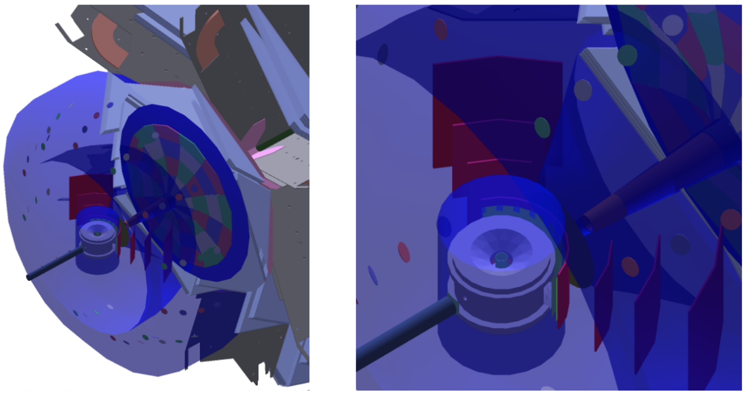

Fig. 18: Concept of the RGH recoil detector in front of CLAS12 HTCC detector.

Such a detector does not pose a specific technological challenge. It can be derived from developments with comparable spatial and time resolution already ongoing for the CLAS12 upgrade in luminosity, and for the ePIC detector at EIC. The area to cover is limited, resulting in a manageable number of readout channels, of the order of 10k for tracking and 1k for TOF, see Sec. 4.3.3. The development effort and construction costs can be minimized by borrowing part of the readout electronics.

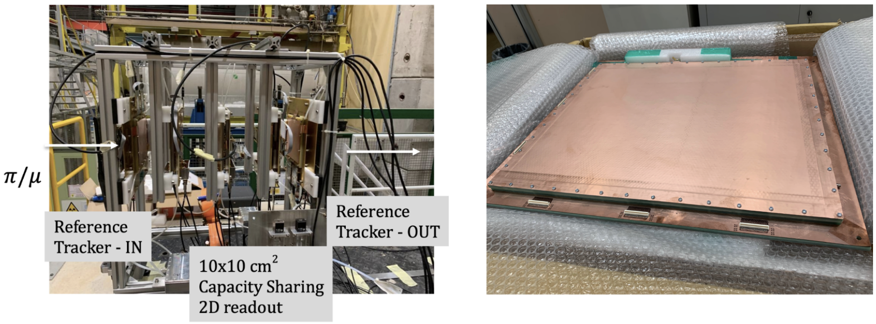

Fig. 19: Set-up used for testing the μRwell performance during a test-beam at the SPS North Area H8C at CERN in June 2023 (left). Large area 40×46 cm^2 μRwell prototype with a 2D cathode readout.

The tracking detector can be derived from the ongoing CLAS12 high-luminosity and ePIC tracking projects based on the μRwell technology (Sec. 4.3.1). Several 10×10 cm^2 prototypes have been produced at INFN with 2D reading layout of ≈ 0.5 mm strip pitch, approaching a spatial resolution close to 100 μm and a time resolution better than 10 ns, see Fig. 19 (left). The maximum width of the current μRwell foils is 620 mm and therefore compatible with the RGH dimensions. A large area 40×46 cm^2 prototype with a 2D capacity sharing readout has already been realized and is now under test (Fig. 19 right). The readout can be largely borrowed from the readout of the GEM chambers produced at INFN for SBS in Hall A, that are currently stored as spares but will become available after the SBS run. This readout is based on the APV25 chip, the chip used for the ongoing μRwell prototype tests. As a backup solution, the readout under study for the high-luminosity project, based on the VMM3 chip, can be adopted.

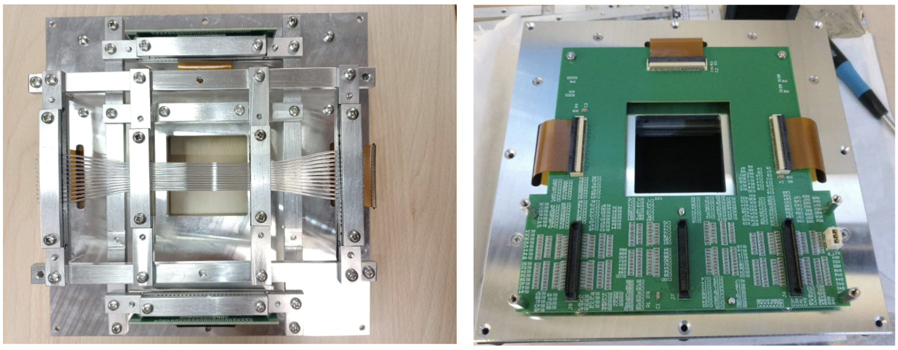

Fig. 20: The scintillating fiber tracking prototype under construction.

To improve the time resolution to a sub-ns level, a plane of scintillating bars readout by SiPMs can be used. Scintillating technology is already well in use at CLAS12 for the Forward and Central Time-Of-Flight systems (FTOF and

CTOF) and the Central Neutron Detector (CND). The SiPM sensors offer a compact and cost-effective solution, that is insensitive to the magnetic fringe fields. Resolutions better than 100 ps have been obtained with fast scintillating rods of a few millimeters thick, 10 mm wide, and of variable length [94, 95]. Prototypes based on fibers and rods are being realized at INFN, see e.g. Fig. 20 (left). The readout can be derived (and largely borrowed) from the one of the CLAS12 RICH detectors, based on the MAROC3 chip, see Fig. 20 (right). This readout has already been successfully used with SiPM matrices for detecting signals down to a few photo-electrons, achieving a single-photon time resolution of 0.5 ns, largely driven by the FPGA settings. A new firmware is available to push the time resolution to better than 100 ps, provided that a proper clock distribution is implemented, as achieved by the ALERT readout. As an alternative, a minimum front-end electronics can be designed to match the ADC/TDC readout modules of the CLAS12 timing detectors that are not in use during RGH (CND, CTOF), although this may limit the total channel number.

4.3.1 μRwell Tracking

The modern photolitographic technology on flexible and standard PCB supports has allowed the invention of novel and robust micro-pattern gas detectors (MPGDs), such as GEM [96], THGEM [97, 98] and Micromegas [99]. These detectors exhibit good spatial and time resolution, high rate capability, large sensitive area, flexible geometry, good operational stability and radiation hardness. However, due to the fine structure and the typical micrometric distance of their electrodes, MPGDs generally suffer from spark occurrence that can eventually damage the detector. The micro-Resistive WELL (μRwell) is a compact, simple and robust MPGD developed for large area applications requiring the operation in harsh environment [100]. The detector amplification stage, similar to a GEM foil, is realized with a polyimide structure micro-patterned with a blind-hole matrix, embedded through a thin Diamond-Like-Carbon (DLC) resistive layer with the readout circuit board (PCB). The introduction of a resistive layer mitigates the transition from streamer to spark and gives the possibility to achieve large gains ($> 10^4$) in the presence of high particle rates (up to 10 MHz/cm^2) [101].

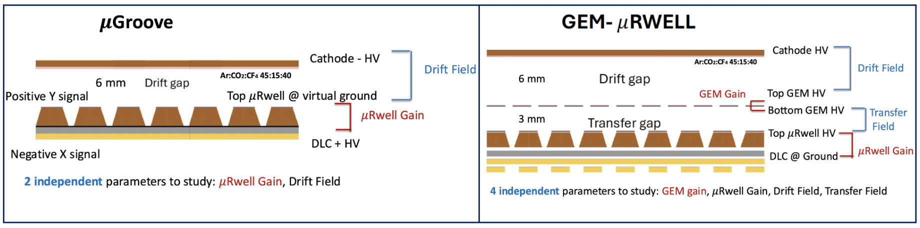

Fig. 21: Alternative architecture under test for obtaining a 2D readout within the same μRwell chamber: Split cathode with a micro-groove plate (left) and GEM-μRwell COMPASS-like stack (right).

The μRwell technology aims to provide micro-pattern gas detectors with performance similar to GEMs but more robust architecture against sparks thanks to the resistive cathode layer. It was originally developed at INFN and is currently under study for the high-luminosity upgrade of CLAS12 and for the inner tracking of ePIC at EIC. The ongoing R&D at INFN has goals that are consistent with the RGH requirements. These are time resolution better than 10 ns, space resolution better than 150 μm, efficiency greater than 95%, low material budget (of the order of 1% χ_0). Different solutions are being studied to obtain an optimized 2D (x, y) strip readout within the same chamber with a discrete pitch dimension (of the order of 0.5 mm to contain the number of channels) and sufficient gain. Prototypes have been realized to test the realistic performance in lab and with beam tests. Prototypes of $10 \times 10\,\mathrm{cm}^2$ have been tested in pairs to compare the relative performance. Large prototypes of $40 \times 46\,\mathrm{cm}^2$ area, comparable with the RGH needs, were also successfully produced. Among the tested options, there is a capacitive sharing readout, a top-segmented readout with a segmentation of just the copper layer of the multiplication stage, or the μGroove readout with a fully grooved multiplication stage, see Fig. 21 (left). They typically meet the specifications only at voltages above 600 V, when the chamber becomes unstable. Promising results have been obtained with a GEM-μRwell COMPASS-like readout, see Fig. 21 (right). In the latter case a gain of $5 \cdot 10^4$ and an efficiency of 97% was obtained at safe voltages around 550 V. The efficiency was measured to be pretty uniform over the detector surface.

The μRwell readout has been studied with the reference APV25 chip that has been a standard for several years [102]. The APV25 is a 128-channel analogue pipeline chip that provides signal sampling with a typical time bin of 25 ns. The basic time information is provided by the sample with the maximum signal amplitude. In order to improve the time resolution, an analysis of the signal shape out of all the recorded samples is required. In this case, a time resolution comparable or better than 5 ns can be obtained. In the basic charge-centroid method, the centroid of the cathode signals is used to estimate the position of the impinging particle. It is typically accurate only for trajectories close to 90 degrees with respect to the tracking plane. The μTPC method attempts a more sophisticated analysis to infer the particle angle from the distribution in time and space of the distributed anode signals. It requires adequate time and space resolutions to properly correlate the information. This was demonstrated with the GEM-μRwell prototypes readout by APV25 at the CERN test-beam, see Fig. 22.

The RGH baseline solution is an architecture based on the well-known APV25 chip and derived from the existing GEM tracker development for Hall-A SBS. The front-end APV card mounting the chip features 128 analog channels, 40 MHz (25 ns) signal sampling, up to 130 analog sample pipeline per channel, 3.4 μs trigger latency, and 100 kHz rate multiplexed readout, see Fig. 23. Up to 16 APV cards (2048 channels) can be connected via HDMI cables to a single MPD VME board. The MPD mounts an Arriga GX FPGA with 128 MB DDR2-RAM and provides FIR filter, common mode and pedestal subtraction, zero suppression, remote configuration, and 2 ns trigger resolution, see Fig. 24. Up to 32 MPDs can be connected to a single SSP module via optical fiber links. The SSP module has been developed by the JLab fast-electronics group and is already in use in CLAS12 for the RICH readout.

The SBS readout electronics and firmware have been developed by INFN in collaboration with JLab. INFN has available at JLab more than 270 APV cards (35000 channels) and 24 MPD boards that can be re-allocated after the end of

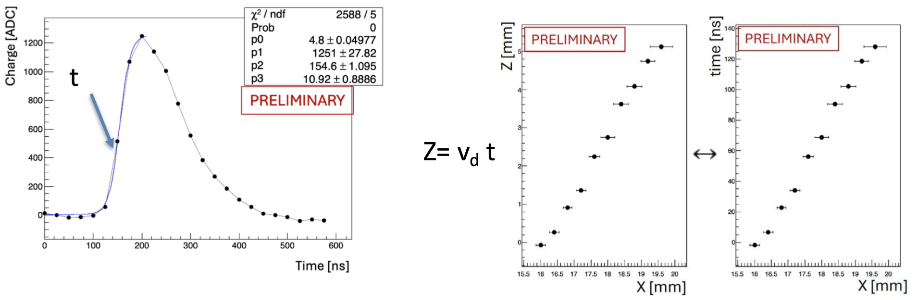

Fig. 22: Example of fit of the μRwell sampled signal to maximize the time resolution (left) and correlation in time and space obtained with the μTPC method (right).

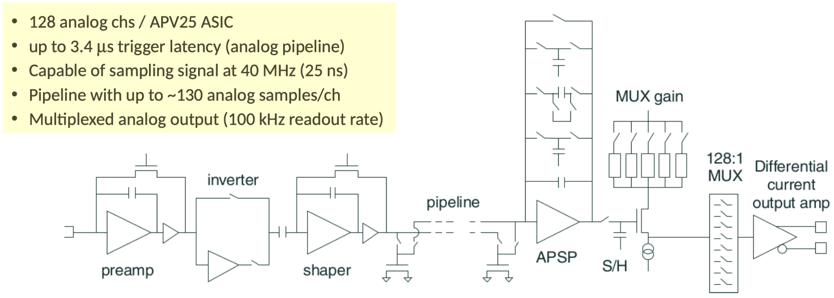
- 128 analog chs / APV25 ASIC
- up to 3.4 µs trigger latency (analog pipeline)
- Capable of sampling signal at 40 MHz (25 ns)
- Pipeline with up to ~130 analog samples/ch
- Multiplexed analog output (100 kHz readout rate)

Fig. 23: The APV25 chip logic diagram and main features.

the SBS run. INFN has also available one VME/VSX crate and a SSP module. The main INFN groups and experts involved in the SBS tracker readout, INFN-RM1 with Evaristo Cisbani and INFN-GE with Paolo Musico, are part of the RGH recoil project and will support its development. An example is the work in progress to develop a new version of the MPD module. Beyond an upgrade to more modern and powerful FPGAs, the new module aims to move from VME to 1GB/s Ethernet connection, support a trigger rate up to 30 KHz with an increased number of samples, and provide new cabling options for the APV25.

The VMM3 chip foreseen for the CLAS12 high-lumi upgrade offers a backup solution for the readout. INFN personnel at INFN-GE involved in the development of a readout chain based on this chip is part of RGH.

The SBS front-tracker has an expected rate up to 500 kHz/cm^2 and an estimated strip occupancy of 60%. With 3 samples per event and a trigger rate of 5 kHz, the MPD-SSP chain has to be able to handle a 100 Mb/s transfer rate. To this goal, no more than 15 APV cards have been connected to the same MPD. The RGH specifications are less stringent. At the foreseen $5{\cdot}10^{33}$ cm^{-2}s^{-1} luminosity, the expected rate in the RGH recoil detector planes approaches a value close to 300 kHz/cm^2 only in the sheet-of-flame region along the bending plane of the magnet, see Fig. 25 and Sec. 4.3.4. In the rest of the detector, the rate is one order of magnitude lower.

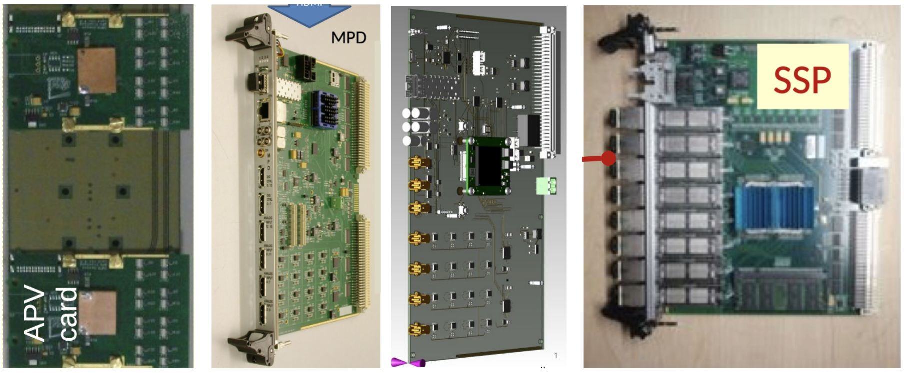

Fig. 24: The essential elements of the SBS tracker APV25 readout chain: the APV front-end card (left), the MPD FPGA board in the existing version and in the upgraded version under development (center) and the SSP data-acquisition module (right).

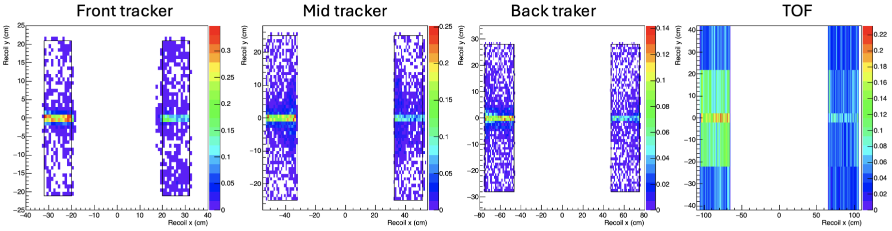

Fig. 25: Expected background rate on the RGH recoil detection planes expressed in MHz/cm^2 for tracking (first three panels) and MHz/ch for TOF (last panel).

4.3.2 Scintillation Timing

The main requirements for the RGH recoil timing detector are, in addition to a O(100 ps) time resolution, a compact layout to fit into the HTCC envelope while maximizing the acceptance, and a flexible tessellation to provide matching with μRwell tracks and control of the background accidentals.

The baseline solution is a plane of scintillating bars readout by SiPM sensors. This technology is well known thanks to the studies connected with Medical Imaging [103], and does not require innovative developments to achieve the wanted time resolution once coupled to the right readout electronics [104].

Contained scintillator dimensions naturally mitigate the dependence of the time resolution on the bar geometry and particle impact point. The scintillation light yield is driven by the bar thickness, but the usable light fraction is ultimately dictated by the active area coverage of the bar rim. Being compact, SiPM does not require large thicknesses. Time resolutions better than 100 ps were reported with bars of 5 mm thickness and variable length up to 20 cm [94] and more recently even with bars of 3 mm thickness and 30 cm length [95]. This performance has also been reproduced with full simulations including optical photons for the geometry utilized here. In case of need, more than one

SiPM can be connected in series to cover a large rim area while containing the number of readout channels.

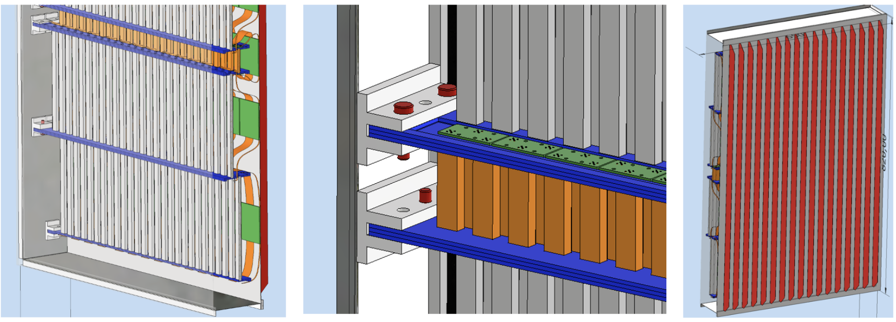

Fig. 26: Concept for the RGH recoil TOF. The timing wall is composed by arrays of vertical scintillating bars readout by SiPMs with the front-end electronics mounted on the downstream support structure (left). Detail of the frame fixing the bars and mounting the sensors (center). The support structure provides cooling and services (right).

Because just a coarse space information is required to match the recoil track, the bar dimensions can be chosen to mitigate the rate of background accidentals. The current design assumes vertical bars with a width of 12 mm and two lengths: 40 mm across the bending plane where background concentrates, and 200 mm outside it. In this way the accidental rate is limited to be below 200 kHz per readout channel, see Fig. 25. The recoil TOF concept is depicted in Fig. 26. The scintillating bars are staggered into arrays and readout on both ends by SiPMs. The bars are vertical to provide best space segmentation in the target magnet bending plane. The timing wall is composed by five arrays of bars whose height is optimized to cope with the background level. The readout electronics are mounted on the downstream supporting structure that provides heat dissipation and services. The front window is minimized in material budget but conductive to provide a Faraday cage. The bars are staggered in order to avoid any dead area due to wrapping or in the region close to the readout electronics.

The readout of the RGH timing SiPMs can be adopted from existing realizations at CLAS12. The easiest solution is to use the spare RICH electronics based on the MAROC3 chip, which is designed for small signals and has been successfully coupled to SiPM in the R&D phase. This chip was successfully run for years at CLAS12, for a Cherenkov application that requires single-photon sensitivity. In the RICH readout, the discriminated signals are fed into a FPGA with an implemented digital TDC with a time bin of 1 ns. A better time resolution was not required for RICH but it can be improved with an existing firmware upgrade (developed for ALERT, see below). However, the clock distribution architecture, based on optical fiber links and the SSP module, would limit the resolution to something around 100 ps, with a contribution comparable to the sensor.

A better solution is the reuse of the ALERT board design done at JLab and based on the PETIROC chip. PETIROC2 has 32 analog input channels that are independently managed and a dynamic range more suited to a multi-photon regime than MAROC. Each channel is divided into two signals, one for time stamping using a TDC and one for charge measurement. The time branch of each channel is preamplified before it is fed into the TDC developed using a leading edge in addition to a Time-to-Amplitude converter. The time bin is 25 ps resulting in a resolution better than 40 ps, with a latency greater than 10 μs. The charge of the pulse is obtained storing the shaped signal values at its peaking time using a switch capacitor array (SCA). The peaking time is defined with respect to a delayed trigger signal produced by the time branch. The ALERT board, see Fig. 27, mounts two PETIROC chips and drives 48 channel SiPM inputs with an individual bias $\approx$1V trimming. It mounts the same FPGA utilized in the CLAS12 RICH readout with an upgraded TDC firmware of 16 ps bin ensuring an intrinsic time resolution better than 35 ps. In the low-noise time-over-threshold readout mode, it can record a measurement proportional to the input charge. The low noise amplification and discrimination chain allow low thresholds ($\approx$ 40 fC) well matched to the expected signal. The clock distribution is done via an ethernet link that preserves a global readout time resolution of about 50 ps, adding a marginal contribution to the one of the sensor.

The development of the recoil ToF detector is synergistic with the R&D activities for a KLM-like detector at the EIC [105] and pursued by the Duke group. This detector would also use scintillator bars with a direct SiPM readout optimized for timing resolutions better than 100 ps. Currently, simulations for this detector are well advanced and being adapted for RGH. Similarly, a front-end board holding the SiPMs and its amplifier circuit developed within KLM can serve as a benchmark and backup solution for the RGH recoil. Planned cosmic ray test stands for the KLM can also be used for the development of the proposed TOF detector.

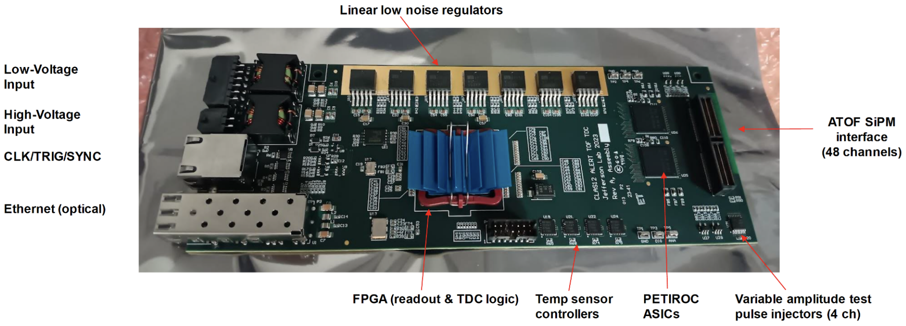

Fig. 27: The ALERT readout board designed by the fast-electronics group at JLab.

4.3.3 Recoil simulation and reconstruction

A full simulation of the RGH recoil detector was implemented in GEMC, the GEANT4-based simulation package of CLAS12. Consistently with the other subdetectors of CLAS12, the geometry of the tracker and of the TOF was defined in the "common-tools" section of Coatjava (the CLAS12 reconstruction software). This ensures automatically that both the simulation and the reconstruction refer to the same geometry. The materials were defined in GEMC. For the tracker, the example of the CLAS12 high-luminosity μRwell chambers was followed (Fig. 28), and a two-dimensional readout with perpendicular strips in x and y was adopted.

Fig. 28: The layers of material implemented in GEMC for the μRwell tracker.

Figure 29 shows the recoil detector as portrayed by interactive GEMC, with the tracker in purple and the TOF in red.

The GEMC digitization of the tracker adopted the same parameters (gain, drift velocity, time resolutions) that were established for the high-luminosity upgrade μRwell chambers. For the TOF, the digitization parameters were derived from detailed simulation studies carried out by the Duke group for the development of the EIC KLM-like detector. In each of the two sectors, the tracking planes are 3 μRwell chambers with 2D readout and 1 mm strip pitch to optimize space resolution. The two TOF planes consist of vertical scintillator rods with 10 mm width and 5 mm thickness to achieve 100 ps of time resolution. To contain accidentals hits and some basic spatial correlation, the rods are organized in 5 rows of two lengths (40 mm in the bending plane, and 200 mm outside). Each rod is readout by two 3×3 mm^2 SiPMs attached at the center of opposite rims. The rods are staggered to preserve acceptance over the sensor location, see Fig. 26. This geometry results in the number of channels outlined in Table 3.

Plane	Name	x Strip (mm)	y Strip (mm)	Channel N.
1	Front tracker	1	1	1276
2	Mid tracker	1	1	2086
3	Back tracker	1	1	2900
4	Time-of-flight	10	40 and 200	1260

Tab. 3: Granularity and number of readout channels of the RGH recoil detector planes.

The reconstruction was implemented in Coatjava. For the TOF, hits were created combining ADC and TDC information, and then were grouped into clus-

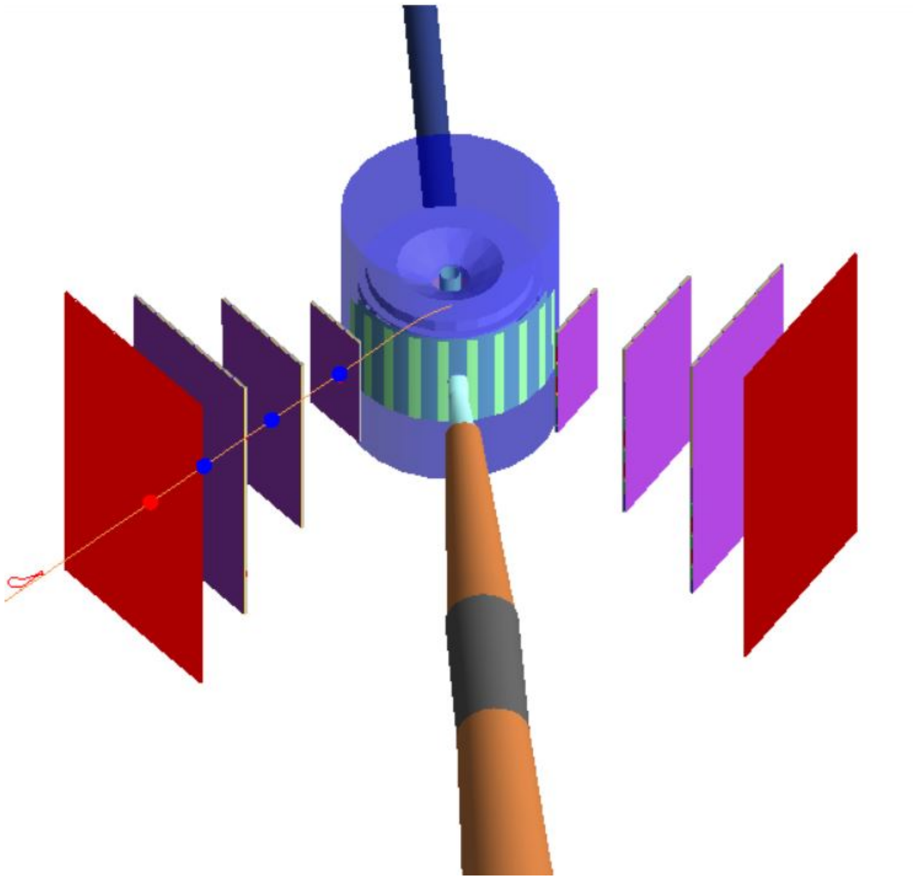

Fig. 29: The recoil detector as shown by interactive GEMC. The tracker layers are presented in purple, and the time-of-flight panels in red. A proton track is visible on the left.

ters using their positions and timing. Similarly, for the tracker hits were created using the strip IDs and their timing information. They were then grouped into clusters, separately for x and for y, and then the x and y clusters were associated into crosses.

For the sake of time and to minimize code complexity, an approximated tracking/reconstruction algorithm was developed. First of all, it was observed that the magnetic field in the region of the recoil detector is so weak that a linear tracking can be implemented among the 3 layers of the tracker and the TOF. This was achieved by looping over all the crosses of each layer, fitting a straight line through each combination of 3 crosses, and choosing the fitted line that gave the best chi2 and was closest to the interaction vertex (obtained from the forward tracking). The intersection ”T” of the fitted line with the TOF panel was determined, the closest TOF cluster to the intersection was found, and its timing was taken to compute β. For the path-length calculation, the intersection ”P” of the fitted line with a cylinder, coaxial with the target magnet, of radius 30 cm was determined (this radius corresponds to where the target magnetic field starts to become non-negligible). The last piece of trajectory was approximated with the segment VP, connecting the interaction vertex "V" and the point P. This approximation, which avoided a lengthy and cumbersome implementation of track swimming in the magnetic field, is of course worse for the lower momenta (stronger bending). The path length was then defined as the sum of the two segments, TP and VP, and β was computed combining the path length and the measured time of flight. The absolute value of the momentum was deduced from β assuming that the track belonged to a proton. In order to determine the momentum components, and thus the angles θ and ϕ at the vertex, the following procedure was adopted:

- We observed that the track does not bend in the xy plane, and therefore the angle ϕ can be obtained from the xy position of the Region-1 cross.
- We found that there is a one-to-one correspondence between the yz components of the momentum and the angle between the fitted track and the line joining the interaction vertex to the cross in Region 1 (Fig. 30). This dependence was parametrized with a polynomial fit and used to deduce the momentum yz component.
- Knowing ϕ, p_{yz}, and p, the other momentum components and the angle θ are computed.

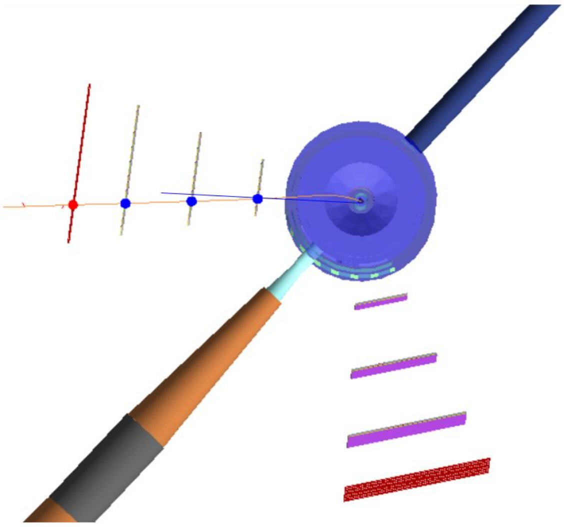

Fig. 30: The angle between the orange line (the fitted track) and the blue line (joining the vertex with the first cross in Region 1) is used to parametrize the momentum component in the yz plane. Figure made with interactive GEMC.

Figure 31 shows the resolutions, defined as the differences of generated and reconstructed variables, in momentum and angles obtained by the recoil detector for simulated protons in DVCS kinematics.

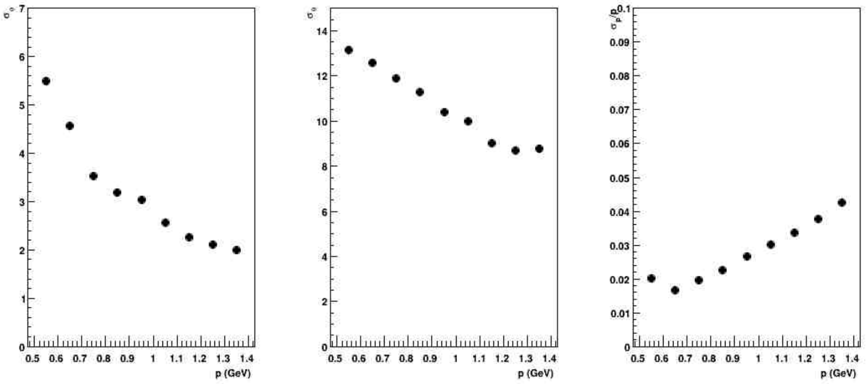

Fig. 31: Angular (left for ϕ and middle for θ) and momentum (right) resolutions, as a function of momentum, obtained with the recoil detector for simulated protons in DVCS kinematics.

4.3.4 Physics Background

A detailed study of background sources was performed using a standardized 252 ns acquisition window around the triggered event, indicating three main components. The first component comes from beam particles losing energy in the target material and bending outside the beam orbit into the detector acceptance, see Fig. 32. They are concentrated in the bending plane of the target magnet and illuminate only one side of the recoil detector, being negatively charged. In most cases the background particle transverses all the recoil projective layers and therefore provides 4 space hits (three from tracking and one from TOF). The second background component comes from shower particles generated in the target region (Fig. 33). These are almost symmetric in charge and therefore illuminate both sides of the detector, but are still concentrated in the bending plane of the target magnet. More than one background particle could be generated in the event, with a recorded hit number which is typically a multiple of 4 (the recoil detector layers). The third background component comes from secondary interactions in the material downstream the target region, especially in the shielding material surrounding the CLAS12 beam pipe (Fig. 34). These low-energy particles have an erratic path with an associated random number of hits on the whole surface of the recoil detection planes.

Preliminary studies indicate that the TOF plane can provide clean seeds for μRwell tracking, thanks to its spatial tessellation and time precision. As a consequence, the recoil trajectory can be properly reconstructed in the presence of the background described above.

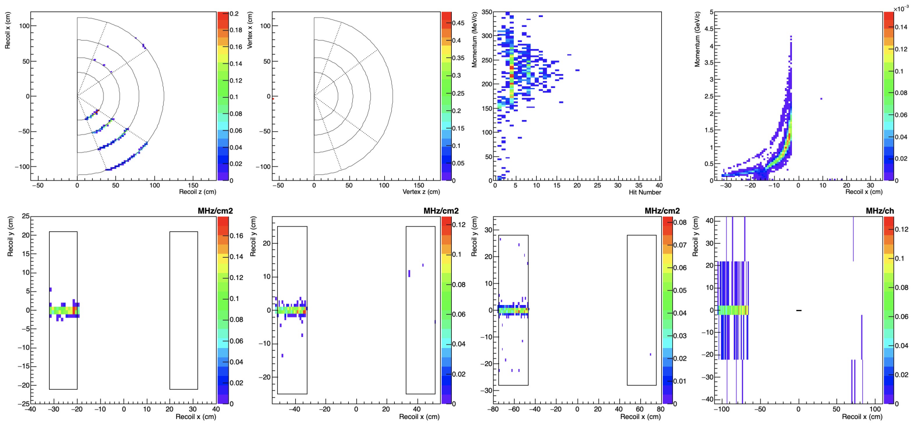

Fig. 32: Expected background on the RGH recoil detection planes (three tracking plus one TOF plane) from beam particles loosing energy into the target material. The top row shows the projection on the bending plane of the recoded hits (left), the location of the originating vertex (center-left), the distribution in momentum and hit multiplicity per particle (center-right) and the correlation between momentum and detected x position on the bending plane (right). The vertex is not visible as far upstream along the beam line. The bottom row shows the background rate (in MHz/cm^{-2} for tracking and MHz/ch for TOF) for the fourth detector layers.

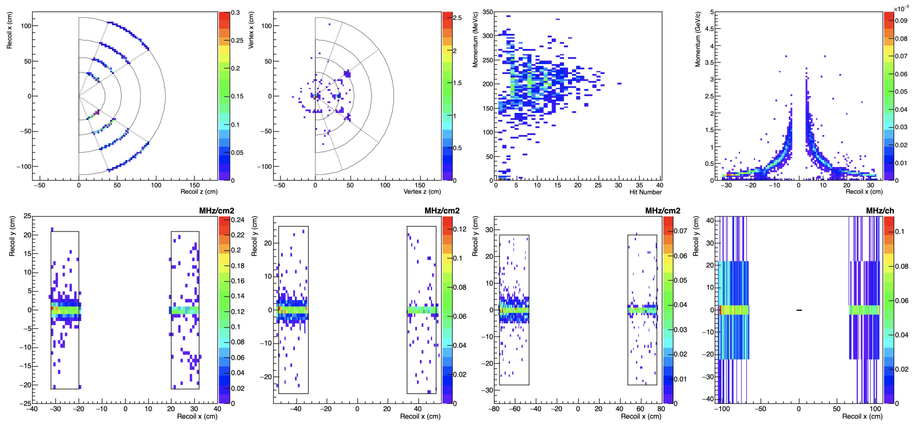

Fig. 33: Expected background on the RGH recoil detection planes (three tracking plus one TOF plane) from shower particle generated into the target region. Panels are organized as in Fig.16.

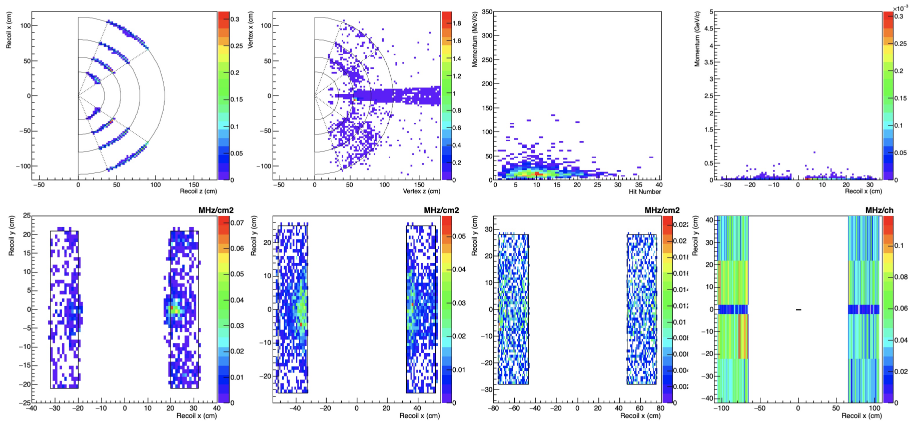

Fig. 34: Expected background on the RGH recoil detection planes (three tracking plus one TOF plane) from secondary interactions downstream the target region. Panels are organized as in Fig.16.

4.3.5 Mechanical model

The cryostat of the RGH target and holding magnet is an adaptation of previous realizations in Hall A and Hall C. It should fit into the clearance of the HTCC detector together with the newly designed recoil detector, see Figure 35. The RGH target position is assumed to stay the same as the current center of the CLAS12 solenoid. The cryostat allows for the exchange of the target and annealing of the irradiated targets in situ. It houses thin aluminum windows for the beam and scattered particles to minimize secondary interactions (Fig. 36). The rectangular exit window is similar to the one realized for the hydrogen target in Hall C.

The RGH recoil detector instruments the region of polar angles between 40 and 70 degrees (Fig. 37). This is the angle interval most populated by recoil protons from DVCS reactions, as shown in Fig. 38. The support structure of the recoil detector will be independent from the target cryostat one in order to allow target maintenance or replacement without any impact on the alignment (Fig. 39).

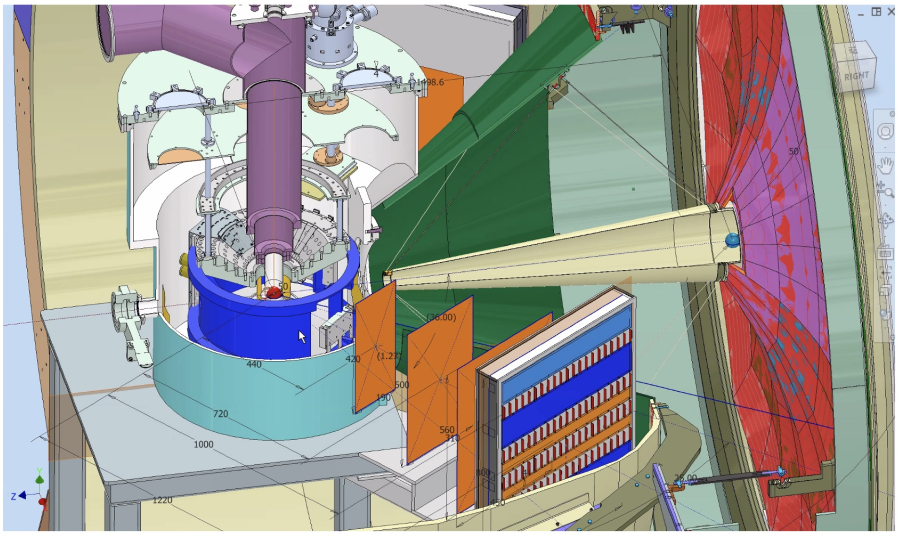

Fig. 35: Overview of the RGH target and recoil system inside the HTCC clearance.

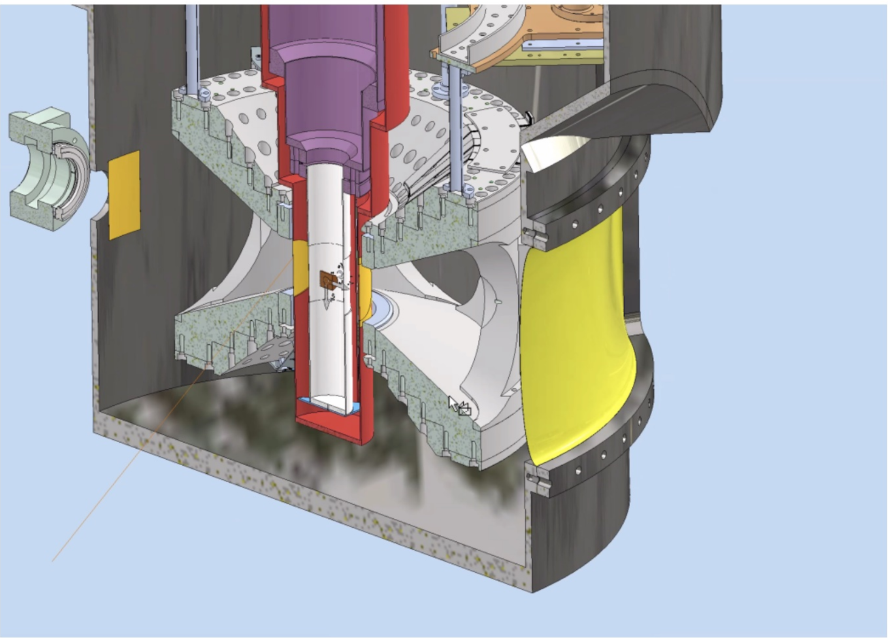

Fig. 36: The entrance and exit windows of the RGH target cryostat.

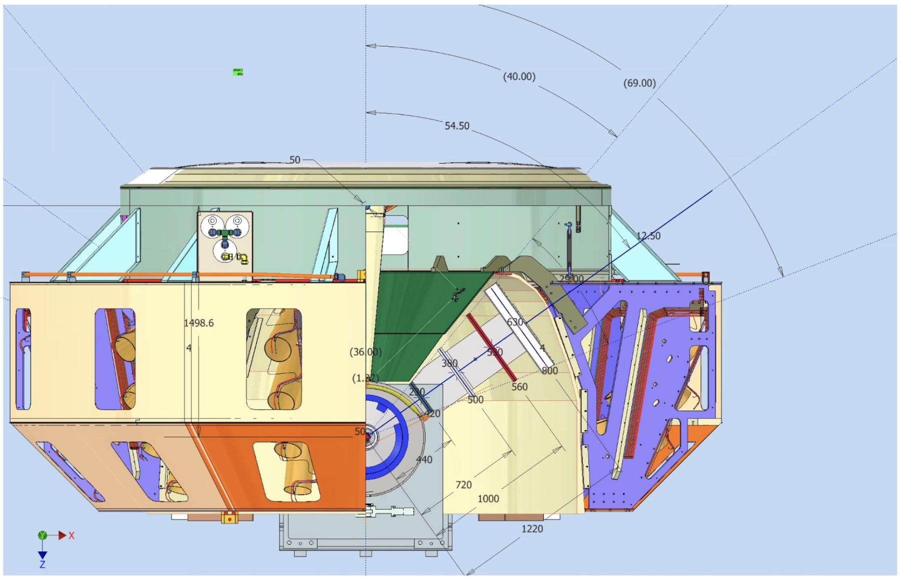

Fig. 37: Top view of the RGH target cryostat and recoil detector showing the clearance and the relevant acceptance angles.

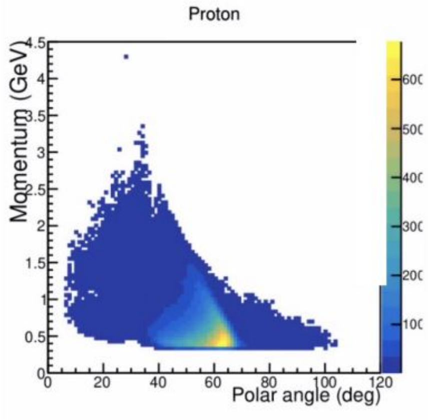

Fig. 38: Momentum versus polar angle distribution of the protons from DVCS events.

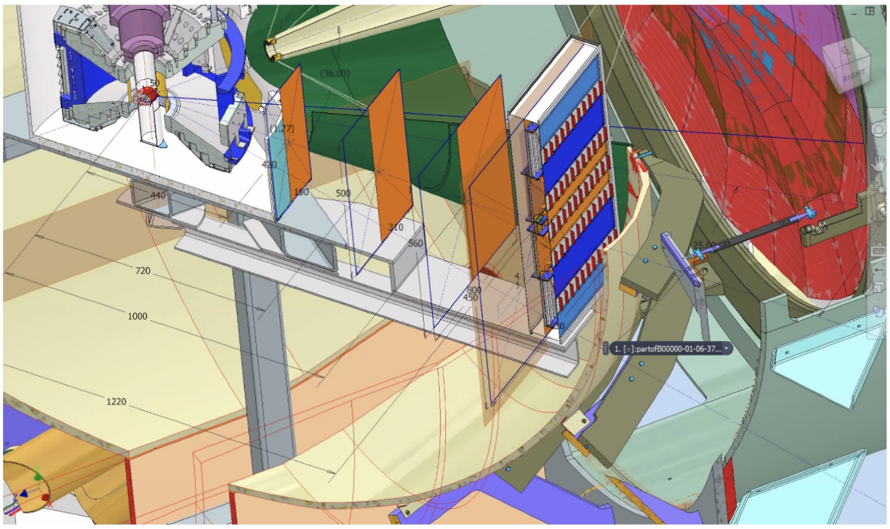

Fig. 39: The support of the RGH recoil detector is a cart able to roll in and out from the HTCC and can be realized without interference with the HTCC.

4.3.6 Available resources

The RGH recoil detector construction is expected to take roughly 3 years and will occur in parallel to the target development as a mainly in-kind user contribution. The time estimate accounts for the detector realization and commissioning, and it assumes that no major electronics development is required thanks to the already existing readout systems and the limited amount of readout channels. Groups already involved in the essential technology R&D are part of the RGH recoil project, see Table 4.

Task	Leading Institution	Expertise
μRwell detector	INFN-RM2, INFN-CT	CLAS12 upgrade, ePIC tracking
μRwell readout	INFN-GE, INFN-RM1	SBS GEM tracking readout
TOF detector	DUKE, Orsay	EIC KLM, CLAS12 CND
TOF readout	INFN-GE, INFN-FE	CLAS12 FT and RICH readout
Mechanics	INFN-LNF	CLAS12 RICH mechanics
Integration	JLab	Hall-B infrastructure and beam

Tab. 4: Main elements of the RGH recoil detector with associated leading Institutions.

INFN-RM2 and INFN-CT work in close contact with the group of Gianni Bencivenni, the inventor of μRwell technology, for the CLAS12 upgrade and the ePIC tracking system. INFN-GE and INFN-RM1 have developed the GEM readout of the SBS experiment. The estimated effort accounts for 6 chambers plus 2 spares, the APV25 readout adaptation to CLAS12 and the possible MPD board upgrade, quantified assuming to connect 15 APV cards to a single MPD as done in SBS, resulting in five new boards plus a spare. Duke is studying a scintillator+SiPM system for the EIC KLM project, while Orsay, that built the CLAS12 Central Neutron Detector, will provide expertise and support for software (simulation and reconstruction). INFN-GE and INFN-FE has experience in SiPM readout for calorimetry and Cherenkov detectors. The effort estimate accounts for two planes of 300 small scintillating bars instrumented by SiPM, the production of 30 PETIROC front-end boards including 4 spares, and the adaptation of existing electronics to RGH needs. INFN-LNF has been responsible for the design of the CLAS12 RICH detector, of its assembly, installation and initial commissioning; it will be responsible for the design of the recoil detector and will contribute to the design of the cryostat. The mechanics and integration account for the installation tools and the required services (power supply and cabling, gas system, slow control, interlock).

The involved groups ensure adequate expertise and workforce to cover both hardware and software needs.

4.4 Luminosity

The CLAS collaboration has completed experimental runs with liquid hydrogen and deuterium targets, and has reached the design luminosity of $10^{35}\,\mathrm{cm}^{-2}\mathrm{s}^{-1}$ with a deuterium target and 45 nA electron beam current. This is much higher than the nominal luminosity $\mathcal{L} = 5 \times 10^{33}\,\mathrm{cm}^{-2}\mathrm{s}^{-1}$ assumed for the RGH experiments. The ongoing high-luminosity project aims to complement the CLAS12 tracking with a front layer of μ-Rwell detectors, able to improve the spatial resolution and rate capability of CLAS12 tracking in the most critical region close to the interaction point, and support a factor two increase in luminosity.

With a dynamically polarized ammonia target, the luminosity is no longer limited by the target polarization lifetime, but by the background induced on the open-acceptance spectrometer. CLAS12 has measured the hit occupancy levels in the Drift Chambers (DC), the most sensitive detectors, as a function of the beam intensity and solenoid current. The typical occupancy is driven by Moeller scatterings in the target and secondary interactions in the shielding around the downstream beam pipe, in the detector structure and in the air filling the experimental hall. CLAS12 simulations reproduce data within an acceptable 30% level.

For the RGH experiments, where the CLAS12 solenoid is replaced by the target 5T transverse polarizing field, the Moeller backgroud is no longer contained inside the beam pipe, but is mainly trapped inside the target region. The baseline of the RGH experiments is to run with no Forward Tagger (FT-OFF) and with additional shielding elements installed to minimize the secondary interactions.

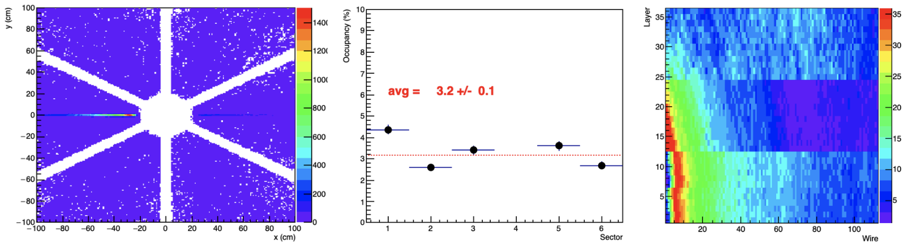

Fig. 40: Simulation results at the nominal RGH luminosity. Background hit distribution on the first DC tracking layer with visible the so-call sheet-of-flame in sector 4 (left). Mean hit occupancy for all DC layers but 4 (center). Hit occupancy per single layer and wire on sector 4 (right).

The RGH background has an additional peculiar component, due to the energy loss of the beam particles passing without interaction through the target. If the loss is big enough, the particle is bent outside the pipe and into the detector acceptance. Such a background is concentrated in the bending plane of the 5T target magnet, creating the so-called *sheet-of-flame*, see Fig. 40 (left). With a vertical magnetic field, the sheet-of-flame will illuminate sector 4 to a level that could be hardly sustainable with the present DC readout, able to record just a single hit in the extended readout gate (between 0.5 μs and 1.5 μs depending on the drift cell size). As a conservative approach, this proposal assumes to switch off the critical DC layers in sector 4 (no tracking), and operate

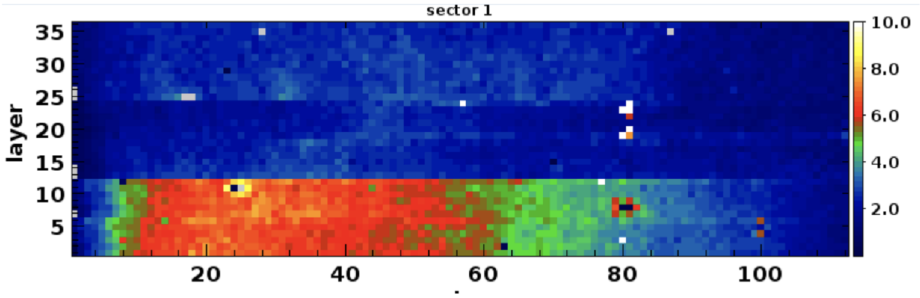

Fig. 41: Typical RGC occupancies as measured by the CLAS12 online monitor during the RGC run with a NH_3 target.

the other sectors up to a maximum tolerable occupancy rate of 6-8% as already achieved (even with higher occupancy hot-spots) during the RGC data-taking on longitudinally polarized NH_3 and ND_3 targets, see Fig. 41. This corresponds to the design RGH luminosity of 5×10^{33} $cm^{-2}s^{-1}$, once a conservative factor of 2 is used to account for the different DC readout gates in simulations, see Fig. 40 (center), and real data.

There are concrete possibilities to exceed the conservative luminosity estimate above. RGH will benefit from the ongoing tracking improvements based on Machine-Learning techniques [106, 107]. With the addition of the μ-Rwell tracking layer under development for the CLAS12 high-lumi project, a significant improvement in luminosity is expected (up to a factor two). Optimization studies are ongoing to adapt the CLAS12 background shielding to RGH. Possible mitigation measures can be introduced to partially operate the critical DC layers in sector 4. These includes switching off just the DC wires close to the beam where the background particles concentrate and compensate with the high-lumi tracking layer, see Fig. 40 (right), veto the events with multiple particles as resolved by the high-lumi tracking layer, upgrade the DC readout to process multiple hits in the readout gate. An interesting option is to rotate the target by 90 degrees in order to align the sheet-of-flame with the torus coil shadow. All these developments are being pursued to maximize the physics output of RGH experiments, with the possibility of improving what has been projected at the time of this proposal.

5 Kinematics

RGH will run with the torus at a nominal current of 3770 A. The solenoid will be off and in parking position. The Central Detector will be replaced by the RGH recoil detector.

5.1 DVCS

In RGH, the recoil proton acceptance is limited in azimuthal angles (to less than ±25 degree) by the target magnet structure. However, the RGH recoil detector has been designed to intercept the most populated interval of polar angles, between 40 and 80 degrees. As a consequence, the phase space coverage is similar to that of RGC, the experiment that used a longitudinally polarized target inside the CLAS12 Central Detector and solenoid (Fig. 42). Figures 43, 44, and 45 show the kinematic coverage in the RGH setup including the proton recoil detector, for the azimuthal versus polar angle of the three final-state particles, for the momentum versus θ, and for the relevant proton-DVCS variables, respectively. Note that Sector 4 is removed from the analysis to produce the DVCS projections (6.2).

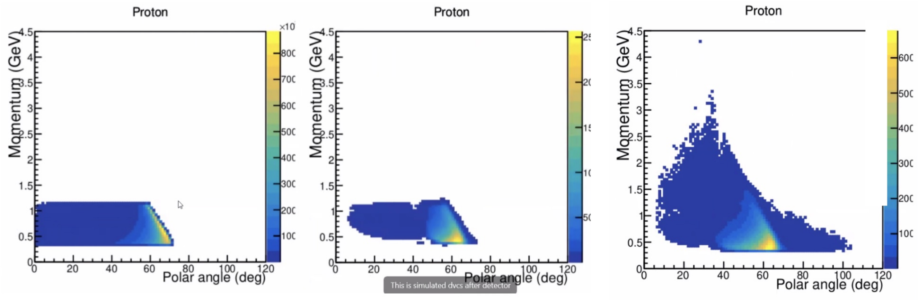

Fig. 42: Proton kinematics in DVCS reaction at 10.6 GeV beam energy. Generated protons (left), protons inside the RGH acceptance (center), and protons detected in CLAS12 during the RGA run (right).

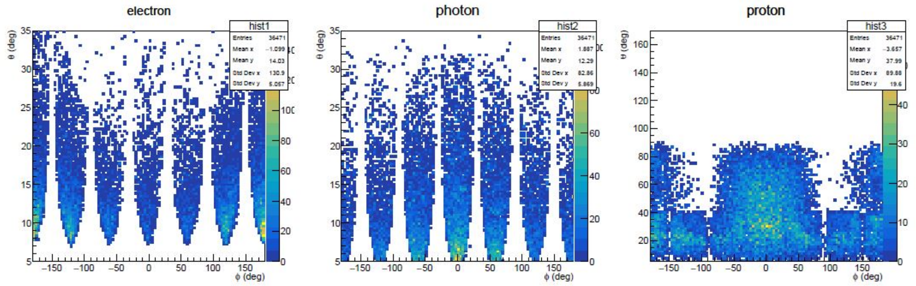

Fig. 43: From left to right: Q^2 vs x_B, Q^2 vs t, and ϕ distributions for proton DVCS events simulated in RGH conditions.

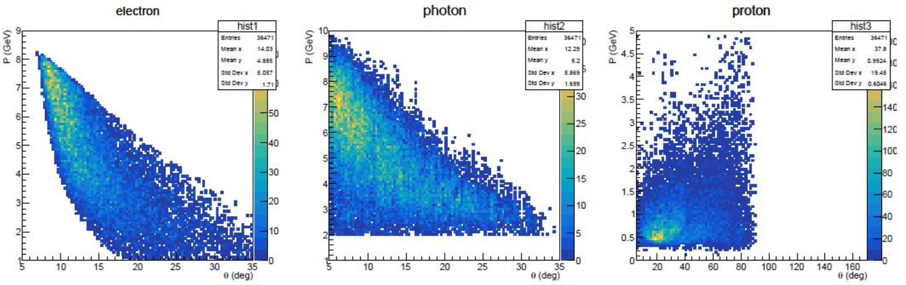

Fig. 44: From left to right: momentum versus θ for electrons (left), photons (middle), and protons (right), for proton DVCS events simulated in RGH conditions.

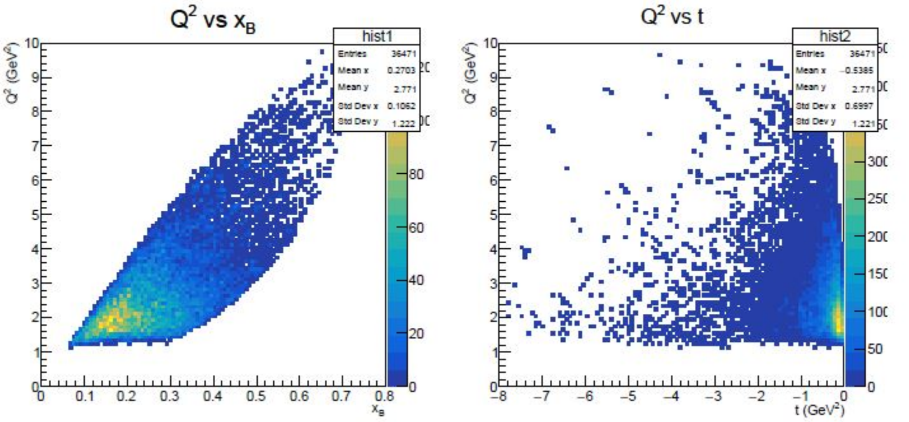

Fig. 45: Q^2 vs x_B (left) and Q^2 vs t (right) for proton DVCS events simulated in RGH conditions.

5.2 SIDIS

The support structure of the RGH target magnet is designed to essentially preserve the forward acceptance and, thus, the SIDIS phase space, see Figure 46. The missing sector (sector 4) does not limit the phase space due to the rotational symmetry of the reaction mechanism, which is defined with respect to the lepton scattering plane. A multi-dimensional binning is possible, covering an extended range in x and Q^2, see Figure 47. In all of the (x, Q^2) bins, there is coverage for the relevant values of the hadron fractional energy z (from 0.2 to 0.8) and the transverse momentum $P_\perp$ (up to 1 GeV/c), see Figures from 48 to 51.

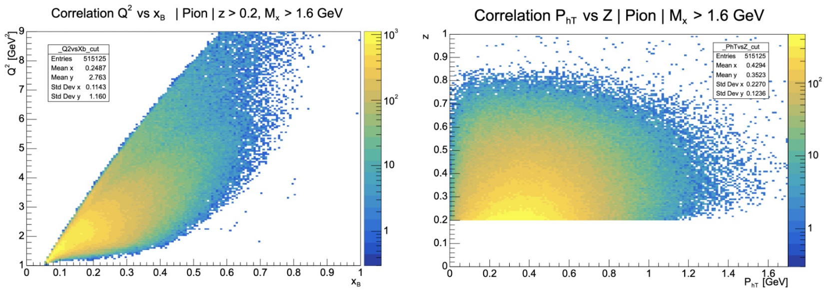

Fig. 46: Q^2 vs x_B (left) and z vs $P_{h\perp}$ (right) for SIDIS events simulated in RGH conditions.

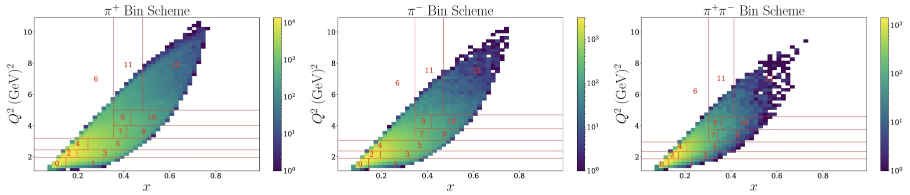

Fig. 47: Possible binning scheme in x and Q^2 for SIDIS events with a leading positive pion (left), negative pion (center) and pion pair (right).

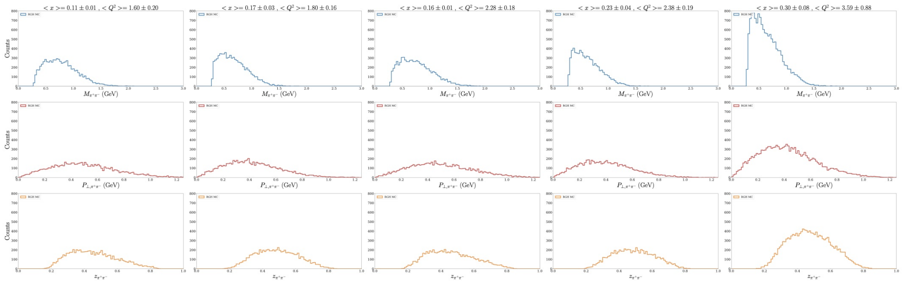

Fig. 48: Distribution of the invariant mass (top row), transverse momentum (middle row) and fractional energy z (bottom row) of SIDIS pion pairs in various (x, Q^2) bins.

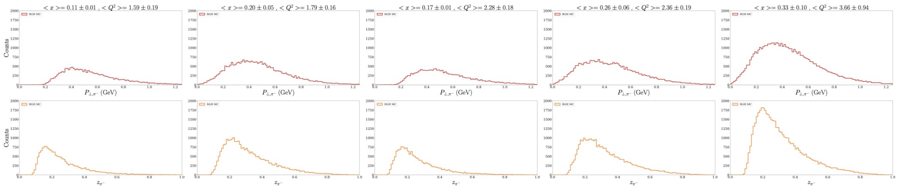

Fig. 49: Distribution of transverse momentum (top row) and fractional energy z (bottom row) of SIDIS negative pions in various (x, Q^2) bins.

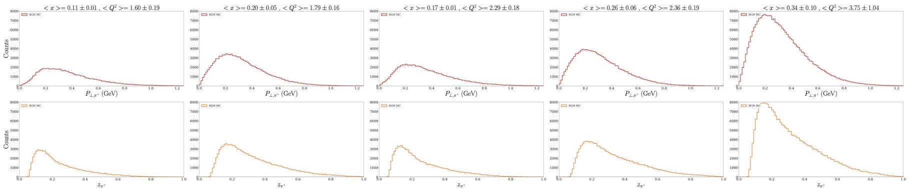

Fig. 50: Distribution of transverse momentum (top row) and fractional energy z (bottom row) of SIDIS positive pions in various (x, Q^2) bins.

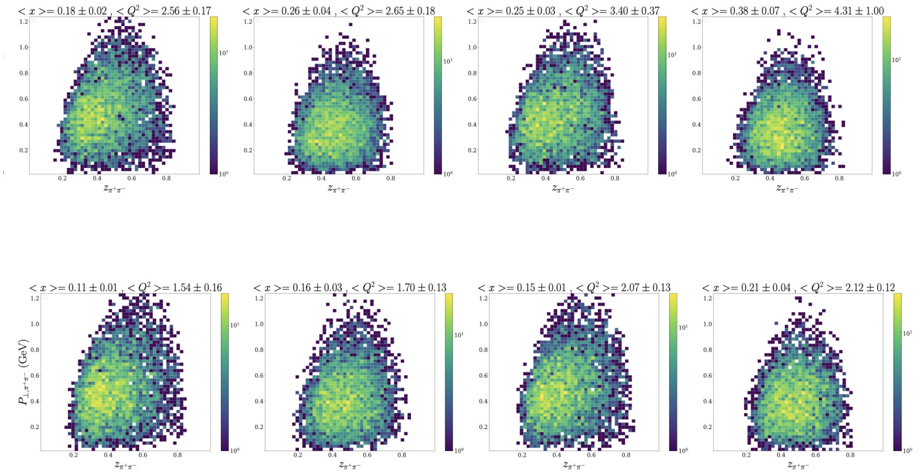

Fig. 51: Correlation between transverse momentum and fractional energy z of SIDIS positive pions in various (x, Q^2) bins.

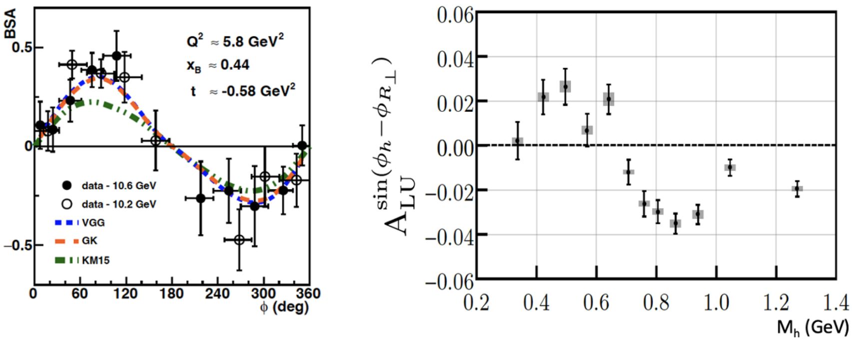

Fig. 52: Examples of CLAS12 published results on beam-spin asymmetry for proton DVCS. Left: DVCS asymmetry as a function of the azimuthal angle ϕ compared to phenomenological models [108]. Right: SIDIS dihadron asymmetry found to be not-zero for the first time [109].

6 Projections

The RGH projections are based on solid ground, as they refer to a running experiment (CLAS12) and a consolidated polarized target technology. The luminosity is not defined by any target irreducible limits, but by the capability in containing the background levels in the experiment, something that is manageable and for which there are many concrete prospects of improvement.

Physics analyses are in progress, using the 10.6 GeV data. CLAS12 results for the SIDIS and exclusive channels have been published by the CLAS Collaboration and presented at conferences. As examples, published beam-spin asymmetries of DVCS events, dihadron and π^+ SIDIS events, based on a fraction of the recorded statistics, are shown in Fig. 52 and Fig. 53 (left), respectively. The data confirm that CLAS12 allows for a much extended reach within the DIS regime (large Q^2) with respect to CLAS and the valence region (large x) with respect to previous experiments, with an unprecedented statistical precision. Thanks to improved knowledge of instrumental effects and the refinement of calibration procedures and reconstruction algorithms, further progress is expected toward the best CLAS12 performances before the start of RGH experiments. For the projections presented here, the full simulation for the RGH setup was used. The number of events was determined from RGC simulations correcting for the ratio of the delivered RGC luminosity to the expected integrated luminosity of RGH as well as the ratio of the acceptances of RGC to RGH.

6.1 Semi-inclusive Physics

Due to the definition of an orthogonal direction, transverse single-spin asymmetries (TTSAs) are key observables for the access of transverse momentum dependent parton distribution functions (TMDs) [111]. The extraction of TMDs is

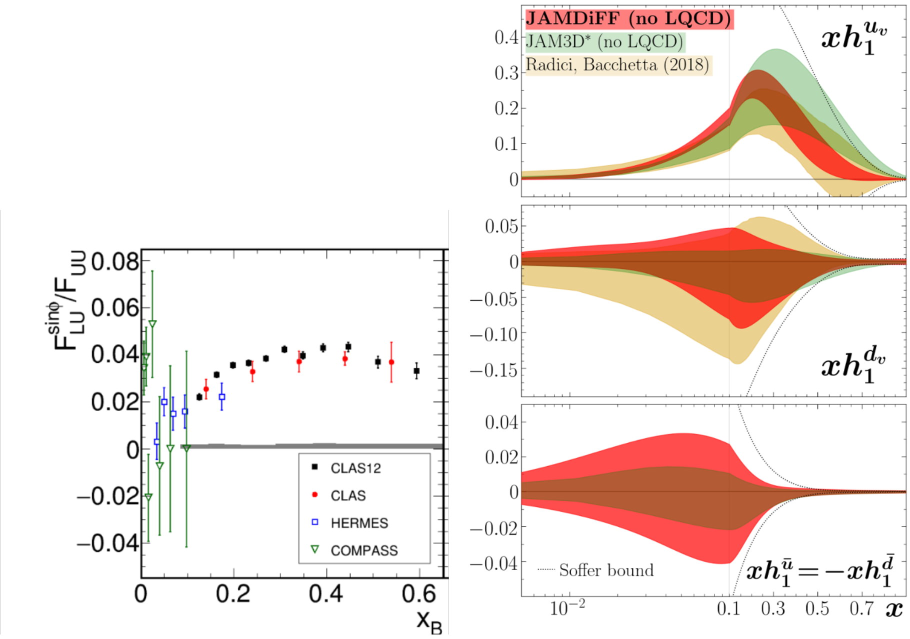

Fig. 53: Left: Beam-spin asymmetries measured by CLAS12 as a function of Bjorken x compared with world data. Figure from [110]. Right: Current extractions of transversity from SIDIS, pp and e^+e^- data. Figure from [22]. Legacy data are mainly limited to $x < 0.3$. This lack of data in the valence region explains the large uncertainty and difference between the transversity extractions.

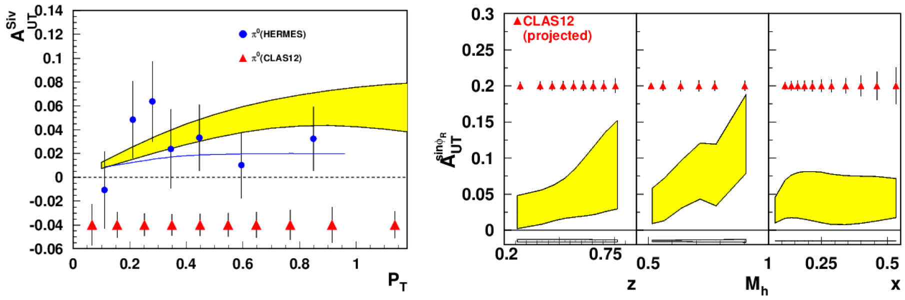

Fig. 54: Left: Projections for the Sivers SSA versus P_T, for a given bin in x and z. The yellow band shows the calculation from JAM3D-22 [12] with relative uncertainty band, and the blue line shows calculations of Pavia group in the kinematical point $x = 0.3$, $Q^2 = 3$ GeV, and $z = 0.4$. The HERMES points are the only existing TTSA measurement for SIDIS π^0 up to now [71]. Right: projected dihadron TTSA as a function of relevant kinematical variables: z, M_h, and x. The yellow band shows the variation of theoretical predictions of the asymmetry due to unknown polarized dihadron fragmentation funcions (DiFFs). The red points show the projected statistical error bars for RGH.

a focus of the nuclear physics community to access the 3D momentum structure of the proton.

Examples of different global extractions of transversity are shown in Fig. 53 (right). The precision of the extractions and their compatibility becomes worse in the valence-quark region. This is due to the lack of data for $x >\approx 0.3$. Since the magnitude of transversity peaks in the same region, this leads to significant uncertainties in the tensor charge, which is the integral of the transversity function over x. The tensor charge can be compared with lattice calculations and is also needed to calculate Beyond Standard-Model phenomena in certain scenarios of new physics with tensor coupling or particle electric dipole moment. World data on longitudinal beam-spin asymmetries (BSAs) compared to the CLAS12 RGA results are shown in Fig. 53 (left). We expect a similar x coverage for RGH, reaching up to $x \approx 0.6$. This would cover the whole peak structure in the current transversity extractions.

Other TMDs like the Sivers function are also likely dominated by the valence region, thus a similar argument for the importance of the CLAS12 TTSAs holds. Recent measurements of BSAs indicate possible strong contributions to inclusive pion spin asymmetries from vector meson (VM) decays. In addition, several JLab proposals have been approved to study longitudinal photon contributions in inclusive pion multiplicities. The Sivers effects also receive a contribution from longitudinal photons, which was never measured or quantified, suggesting that the systematics on the Sivers effect measurements may be currently underestimated. This makes the measurements of all observables in semi-inclusive π^0 production, and the Sivers effect in particular, critical: the neutral pion is known to receive a minor contribution from exclusive VM decays, and, even in the exclusive limit, minor contributions from longitudinal photons. The high statistics of CLAS12 at large x, where the effects are significant, would allow detailed measurements of TTSAs, in particular as a function of the transverse momentum of hadrons. Understanding the transverse momentum dependencies of all kinds of observables in polarized SIDIS, including multiplicities and the Sivers asymmetry, has always been a challenging task for theory, but it is instrumental in providing important information for phenomenological studies and a validation of the underlying dynamics description. The contributions from VM, and the strong correlations between hadrons produced in SIDIS, make the measurements with dihadrons critical for the interpretation of complex observables, such as single-spin asymmetries and transverse single-spin asymmetries in particular. A significant Sivers effect was recently predicted for dihadrons [112].

Data-driven projections for SIDIS observables have been derived following the method explained in Section 6.2, and benefit from the fact that the forward acceptance of pions, and π^0 in particular, is largely preserved. Note that in the SIDIS case, where nuclear interactions (on nitrogen) cannot be kinematically suppressed, the target dilution factor $f = 3/17$ should be treated as polarization and multiply the error instead of the yield.

An example of the projected Sivers asymmetry measurement with CLAS12 as a function of the transverse momentum of neutral pions in a small bin in x is shown in Fig. 54 (left). The projection for a particular transverse single spin asymmetry for dihadrons, providing access to transversity measurements, is shown in Fig. 54 (right).

RGH pseudo-data have been used to estimate the impact on our present knowledge of the flavor-separated tensor charge in the JAM framework using di-hadron asymmetries following the setup described in Ref. [22]. The JAM fit uses a parametrized functional form. To our knowledge is currently no pure unparametrized (neural network) fit for transversity. A consequence is that JAM might underestimate uncertainties on the transversity distribution and thus the tensor charge in kinematic regions where there is no data, thus somewhat underestimating the impact of the CLAS12 data. However, as shown below, even with the current setup, the CLAS12 data has a significant impact on the extraction of transversity and tensor charge and might be able, for the first time, to differentiate between the tensor charge value preferred by current extractions from data and from the lattice. The pseudo-data were derived from existing CLAS12 data accounting for the different acceptance and luminosity of RGH. The expected data will significantly reduce the present uncertainty of the di-hadron asymmetry as shown in Figure 55. Specifically, uncertainties in the valence quark region that dominates the value of the tensor charge will be reduced. Current phenomenological extractions from single and di-hadrons favor different values of the tensor charge from those obtained from the lattice. However, due to the restricted kinematical reach of current datasets, no strong conclusion on the compatibility of data and lattice can be drawn: Without inclusion of the lattice data, the phenomenological fit prefers a value for the tensor charge that is inconsistent with the lattice value. However, including the lattice value as an overall constraint still yields a good description of the data while producing a value of the tensor charge that is consistent with the lattice result. This behavior is interpreted as evidence that the current data cannot make a strong statement if there is agreement with lattice or not. This is likely due to kinematical areas that are not covered by data. This behavior has been seen both, in the single and di-hadron extractions. As shown in Fig. 56, the situation changes when the projected RGH data is included with the assumption that it follows the current best phenomenological extraction from data only. Now the fit including the data prefers a different value of the tensor charge than lattice, even when including the lattice point as an overall constraint. The interpretation of this behavior is that the fit now cannot accommodate the tensor charge value preferred by data and by lattice at the same time. Thus RGH data will be able to differentiate between the tensor charge value preferred by current data and lattice [113].

This demonstrates the impact the projected data will have on our extraction of the tensor charge and the solution of this longstanding issue.

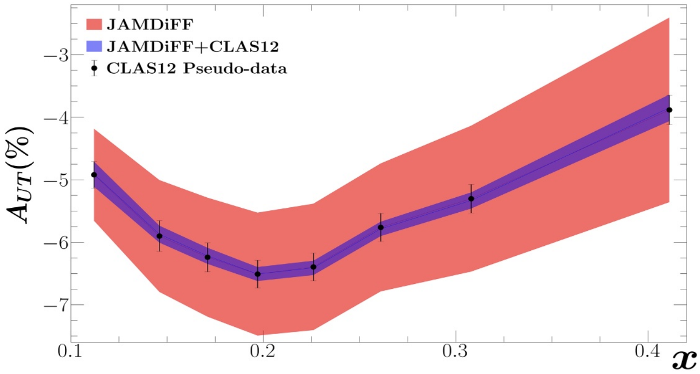

Fig. 55: Impact of the RGH pseudo-data on the JAMDiFF phenomenological fit, from [113].

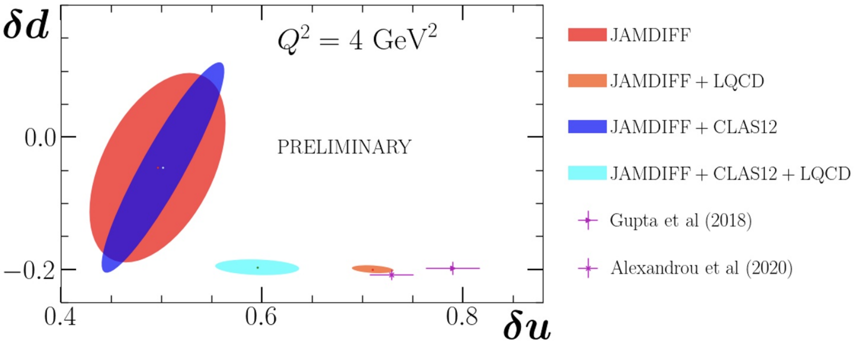

Fig. 56: Impact of the RGH pseudo-data on the tensor charge δu of the u quark flavor, from [113]. The RGH data-set will be competitive with lattice calculations and provide an effective benchmark.

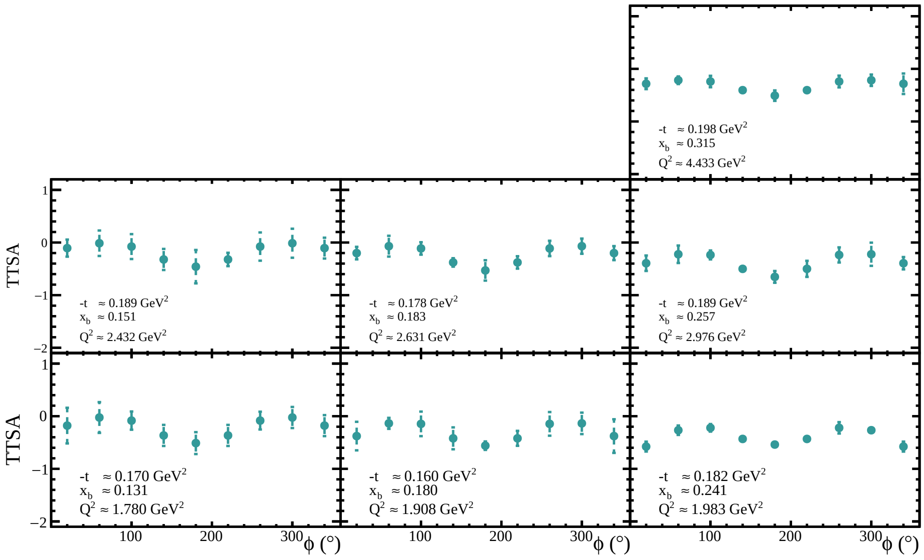

Fig. 57: Projections for the transverse target-spin asymmetry versus ϕ which will be obtained by RGH for the proton-DVCS reaction, for the lowest bin in $-t$, for 3 bins in x_B (along the horizontal axis), and 3 bins in Q^2 (along the vertical). The average kinematics is indicated on each plot.

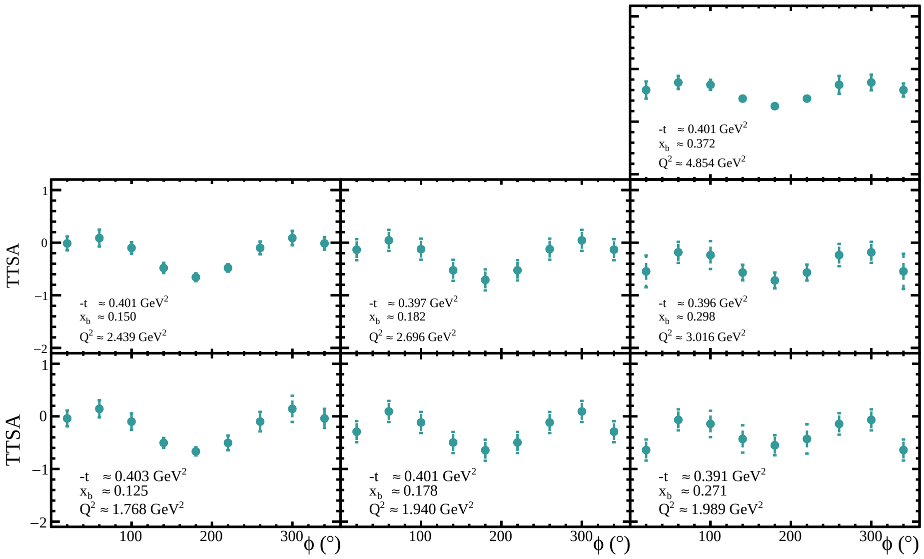

Fig. 58: Projections for the transverse target-spin asymmetry versus ϕ which will be obtained by RGH for the proton-DVCS reaction, for the second bin in $-t$, for 3 bins in x_B (along the horizontal axis), and 3 bins in Q^2 (along the vertical). The average kinematics is indicated on each plot.

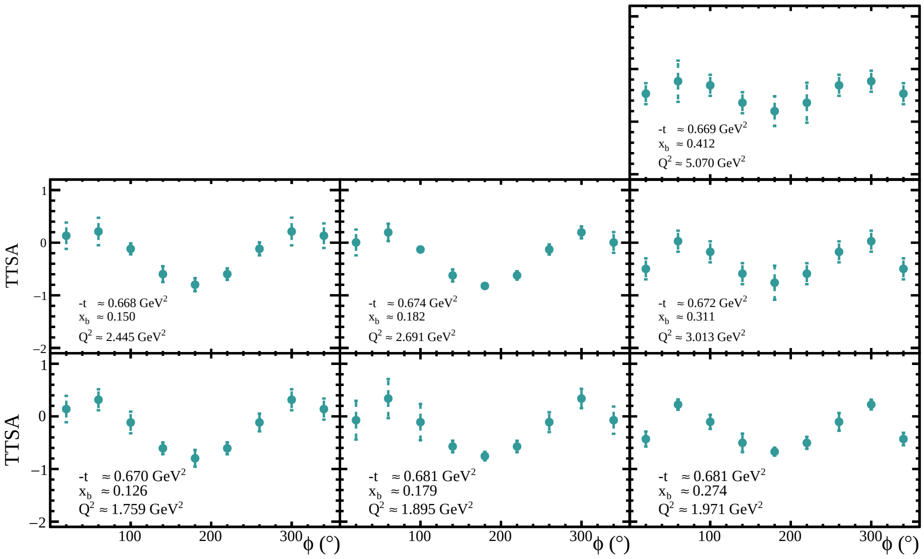

Fig. 59: Projections for the transverse target-spin asymmetry versus ϕ which will be obtained by RGH for the proton-DVCS reaction, for the third bin in $-t$, for 3 bins in x_B (along the horizontal axis), and 3 bins in Q^2 (along the vertical). The average kinematics is indicated on each plot.

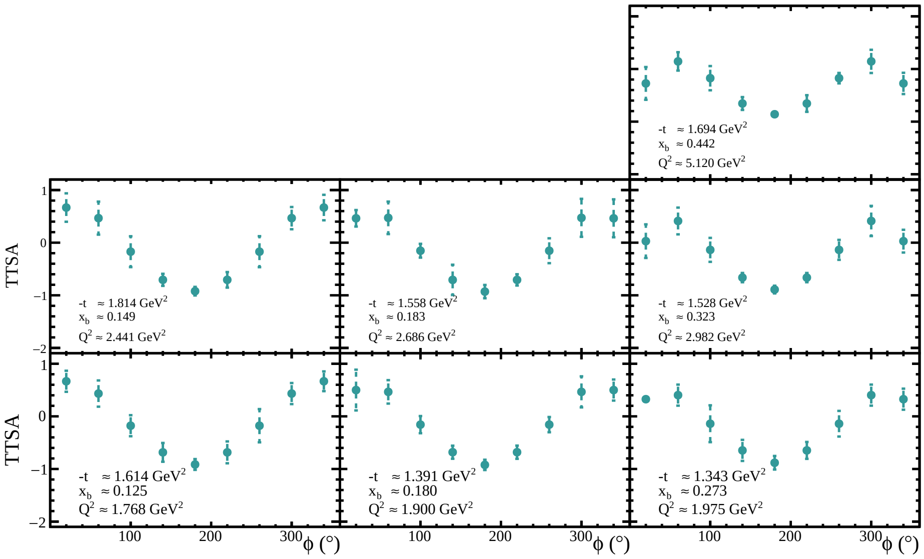

Fig. 60: Projections for the transverse target-spin asymmetry versus ϕ which will be obtained by RGH for the proton-DVCS reaction, for the fourth bin in $-t$, for 3 bins in x_B (along the horizontal axis), and 3 bins in Q^2 (along the vertical axis). The average kinematics is indicated on each plot.

6.2 DVCS

Measuring DVCS on a transversely polarized proton target is crucial as the transverse target-spin asymmetry (TTSA) is the DVCS observable having the strongest sensitivity to the GPD E of the proton. Knowing E is paramount in order to extract the quarks' angular momentum contribution to the proton spin via the Ji sum rule [35].

Projections for the DVCS TTSA that will be obtained by RGH were computed using a data-driven method to estimate the yields. Proton-DVCS yields (Y) were extracted using data from the RGA Fall 2018 period. The acceptances were computed for the RGH and the RGA configurations using an event generator for DVCS in NH_3, the CLAS12 GEANT4-based simulation software, GEMC, and the CLAS12 reconstruction. The simulation for RGH included the full realistic description of the recoil tracker and Time-Of-Flight detector described in Sec. 4.3. The RGA pDVCS yields were multiplied, for each kinematic bin in $(Q^2, x_B, -t, \phi)$, by the ratio of the RGH and RGA acceptance for pDVCS. Then this product was multiplied by the ratio of the integrated luminosities of RGH and RGA. In this way, the projected yields were estimated in a fully data-driven, model-independent way. This is summarized in Eq. 7:

$$Y_{RGH}(i) = Y_{RGA}(i) \cdot \frac{Acc_{RGH}(i)}{Acc_{RGA}(i)} \cdot \frac{L_{RGH}}{L_{RGA}} \cdot \frac{3}{17}, \tag{7}$$

where i labels the 4-dimensional bin in $Q^2, x_B, -t, \phi$, $L_{RGH} = 100$ days $\cdot\, 5 \cdot 10^{33}$ $\mathrm{cm}^{-2}\mathrm{s}^{-1}$, $L_{RGA} = 16$ days $\cdot\, 0.8 \cdot 10^{35}$ $\mathrm{cm}^{-2}\mathrm{s}^{-1}$, and the factor 3/17 accounts for the fraction of protons from hydrogen in NH_3.

The grid of 4-dimensional bins was established according to the statistics obtained with Eq. 7. Then, the TTSA was computed, as a function of ϕ, at the average kinematics of each $(Q^2, x_B, -t)$ bin, using the VGG model. The yields obtained via Eq. 7 for RGH were used to deduce statistical error bars for the TTSA, according to the formula:

$$\sigma_A(i) = \frac{1}{P} \cdot \sqrt{\frac{1 - (P \cdot A)^2}{Y_{RGH}(i)}}, \tag{8}$$

where A is the value of the TTSA, and P is the target polarization, assumed to be 85%, a value consistent with the typical target performances obtained during the Run Group C run. Note that the selection of the exclusive kinematics largely suppress the nuclear interactions (on nitrogen) and therefore the target dilution $f = 3/17$ reduces the yields, but does not suppress the asymmetry as in the case of SIDIS.

In order to test the sensitivity of the projected data on the GPD E, various sets of quark's angular momenta J_u and J_d were used to compute the TTSA with the VGG model. In this model, indeed, J_u and J_d parametrize directly the GPD E, and can be chosen as input parameters.

The projections for the TTSA are shown in Figs. 6.1 to 6.1, plotted as a function of ϕ for each bin in $(Q^2, x_B, -t)$ for the case $J_u = -0.5$, $J_d = -0.1$. Figure 61 shows the transverse target-spin asymmetry versus ϕ for one of the $(Q^2, x_B, -t)$ bins shown in Fig. **??**, and for three sets of values of J_u and J_d (brown: $J_u = 0.5$, $J_d = 0.1$; cyan: $J_u = -0.5$, $J_d = -0.1$; blue: $J_u = 0.2$, $J_d = 0$). The size of the projected error bars allows us to distinguish between the three hypotheses. For comparison, the asymmetry as computed with the PARTONS code is also shown (in black), as a cross-check of the model used to produce the projections.

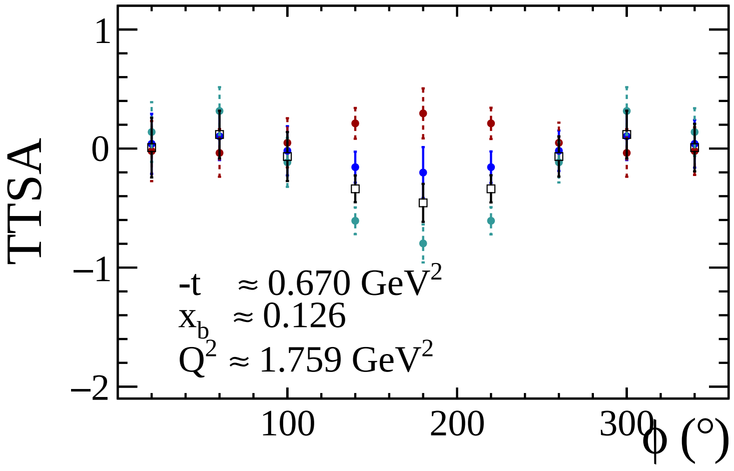

Fig. 61: Projections for the transverse target-spin asymmetry versus ϕ which will be obtained by RGH for the proton-DVCS reaction, for one $(Q^2, x_B, -t)$ bin, and for 3 sets of values of the quark's angular momenta J_u and J_d, as computed by the VGG model. Brown: $J_u = 0.5$, $J_d = 0.1$; cyan: $J_u = -0.5$, $J_d = -0.1$; blue: $J_u = 0.2$, $J_d = 0$. For comparison, in black are shown the values computed with PARTONS. The error bars reflect the expected statistics of RGH.

This is even more evident in Fig. 62, which shows the moments A_{UT}, extracted by fitting the TTSA with the function $A_{UT}\sin(\phi-\phi_S)\cos\phi$. The colors indicate the three sets of values given to VGG for J_u and J_d. Aside from some kinematics for which the expected statistical precision will be poorer, such as at low x_B and $-t$ in the second Q^2 bin, the precision of the data will be enough to discriminate between the various model hypotheses. Moreover, this will be the first time that the TTSA of pDVCS will be extracted in 4 dimensions and on such a vast kinematic coverage. The only existing published data for this observable, measured by HERMES [114], are included in Fig. 62, represented by the 4 black points in the bottom-left plot. The RGH experiment will not only improve on the statistical precision of those particular kinematics but also extend the measurement of the TTSA over a much larger phase-space region. The inclusion of the RGH pDVCS data in global fits for the extraction of GPDs will strongly constrain the poorly known GPD E of the proton. This will allow us, in particular, to map the t-dependence of the imaginary part of the GPD E, and thus to make an important step toward the extraction of the contribution of the quarks' angular momentum to the proton spin via the Ji sum rule.

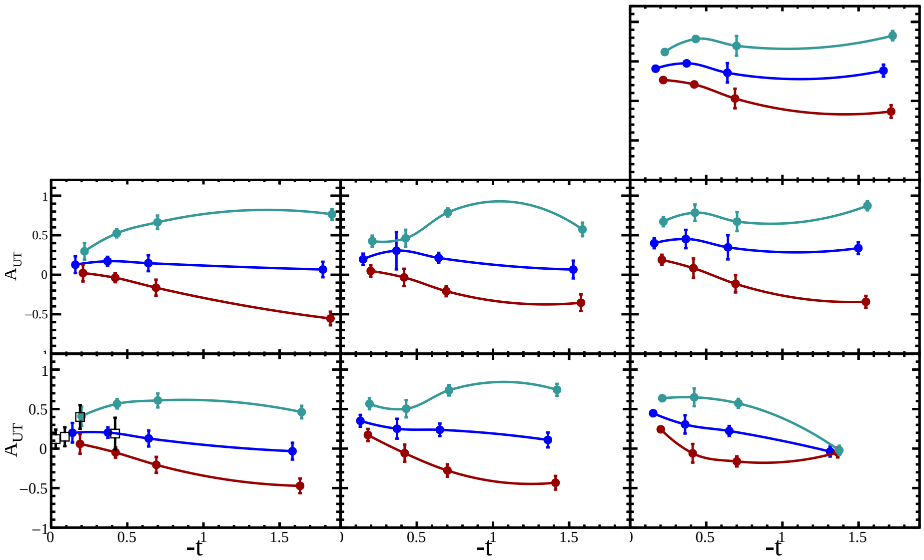

Fig. 62: Projections for the A_{UT} moments which will be obtained by RGH for the proton-DVCS reaction, for the full grid of $(Q^2, x_B, -t)$ bins, and for 3 sets of values of the quark's angular momenta J_u and J_d, as computed by the VGG model. The error bars reflect the expected statistics of RGH. The color code is the same as in the caption of Fig. 61. The 4 black points in the bottom-left plot are the HERMES data [114].

6.2.1 π^0 background

Once the events containing one electron, one neutron and one photon are selected, the pDVCS/BH final state can be isolated by cutting on the missing masses and other exclusivity variables. However, due to the finite resolutions of the detectors, the final event sample will still be contaminated by events coming from the $ep\pi^0$, where one photon from the π^0 decay is detected in the forward calorimeters while the other escapes detection. This contamination will be evaluated and subtracted as was done in previous DVCS CLAS analyses [44, 47, 46, 48], by extracting exclusive $ep\pi^0$ events — detecting both decay photons — from the data, and using Monte-Carlo simulations to evaluate the ratio of acceptances of π^0 events with 1 and 2 photons detected. The final number of pDVCS/BH events, in each 4-dimensional bin, will be obtained as:

$$N_{DVCS}(Q^2, x_B, -t, \phi) = N_{ep\gamma}(Q^2, x_B, -t, \phi) - N_{\pi^0 1\gamma}(Q^2, x_B, -t, \phi) \qquad (9)$$

where

$$N_{\pi^0 1\gamma}(Q^2, x_B, -t, \phi) = N^{data}_{\pi^0}(Q^2, x_B, -t, \phi) \cdot \frac{N^{MC}_{\pi^0 1\gamma}(Q^2, x_B, -t, \phi)}{N^{MC}_{\pi^0 2\gamma}(Q^2, x_B, -t, \phi)}. \qquad (10)$$

Here $N_{ep\gamma}$ is the number of events, in a given 4-dimensional bin, passing the DVCS exclusivity cuts, $N^{data}_{\pi^0}$ is the number of events passing the $ep\pi^0$

exclusivity cuts, $N^{MC}_{\pi^0 1\gamma}$ is the number of reconstructed simulated π^0's passing the DVCS exclusivity cuts, and $N^{MC}_{\pi^0 2\gamma}$ is the number of reconstructed simulated π^0's passing the $ep\pi^0$ exclusivity cuts. An alternative π^0 background subtraction method was adopted in [50], and will be used as a systematic check in the RGH DVCS analysis.

The level of π^0 background in the RGH setup was evaluated as follows: Monte-Carlo $ep\pi^0$ events produced on an NH_3 target were generated and passed through the full GEMC simulation and reconstruction chain, for both the RGH and the RGA configurations. Then the π^0 yield was obtained using the same strategy as in Eq. 7, thus scaling the RGA $ep\pi^0$ experimental yields by the ratio of acceptances of RGH and RGA times the luminosity ratio. Figure 63 shows the obtained projected yields in RGH conditions for DVCS (red), $ep\pi^0$ (black), and the sum of DVCS π^0 (blue), as a function of three exclusivity variables, after applying the following DVCS selection cuts (on all variables except the plotted one): $E_\gamma > 2$, $Q^2 > 1.0$ GeV^2, $W > 2$ GeV, $p_p > 0.3$ GeV, $p_e > 1.0$ GeV, $\Delta\phi < 1.5°$, $\Delta t < 2$ GeV^2, $p_X(ep \to ep\gamma X) < 1$ GeV, $\theta_{\gamma X} < 5°$. By comparing the black and blue histograms of Fig. 63 within the regions of the DVCS selection cuts, the π^0 contamination appears to be roughly 30%. This is consistent with what was typical found in other CLAS12 experiments for the DVCS detection topology with photons in the ECAL, as is shown in Sec. 6.2.2 for the RGC case.

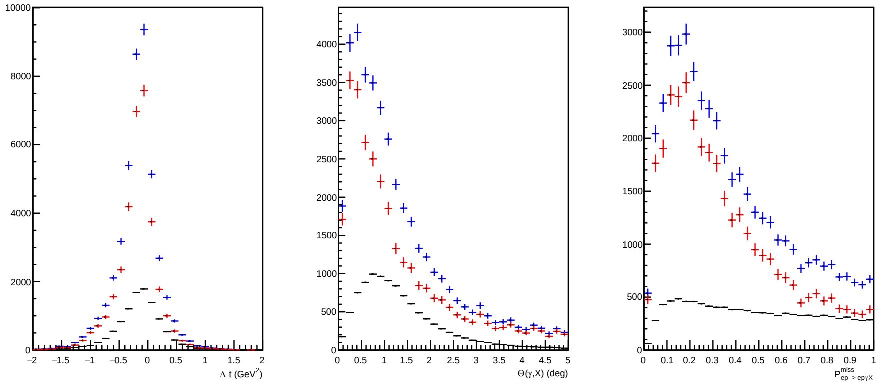

Fig. 63: Projections of yields for DVCS (red), $ep\pi^0$ (black), and DVCS+π^0 (blue), for three exclusivity variables: the difference between two ways of computing the t variable (left), the cone angle between detected and missing γ (middle), and the missing momentum from $ep \to ep\gamma X$ (right). For each plot, the DVCS exclusivity cuts are applied on all variables except the plotted one.

6.2.2 Feasibility of DVCS analysis on polarized NH_3: the RGC example

As previously mentioned, data were recently taken by CLAS12 with a longitudinally polarized target during the Run Group C (RGC) experiment, and a

DVCS analysis on protons in NH_3 is ongoing [115]. One of the three run periods composing RGC (”Fall2022”) had no Forward Tagger to detect photons, as will be the case for RGH. Here below we show some plots from the ongoing preliminary DVCS analysis to support our simulation-based studies and corroborate the feasibility of the extraction of the DVCS events as well as the assumptions we made in our estimate of the systematic uncertainties (Sec. 6.3).

Figure 64 shows the variables used to ensure the exclusivity of the DVCS final state, and the effects of the applied cuts. In particular, the reduction of the carbon data after cuts shows how effective the exclusivity cuts are in removing the nitrogen background. This is also evident from Fig. 65, where the dilution factor for DVCS is plotted as a function of each of the 4 kinematic variables: its value is around 95%. The dilution factor was computed with two different methods yielding very similar results. This motivates our choice of systematic uncertainty in Sec. 6.3.

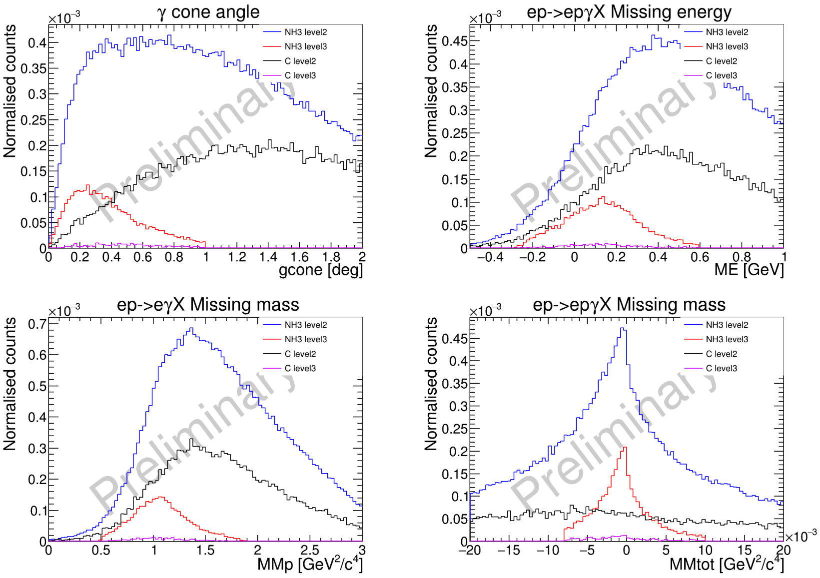

Fig. 64: Preliminary proton-DVCS analysis on CLAS12-RGC data (Fall2022), courtesy of Samy Polcher (CEA Saclay). Exclusivity variables for the selection of the DVCS final state: cone angle between the measured and the missing photon (top left), missing energy of the $ep\gamma$ system (top right), missing mass of the $e\gamma$ system (bottom left), missing mass of the $ep\gamma$ system (bottom right). The colored lines represent the NH_3 data with no cuts (blue), the carbon data with no cuts (black), the NH_3 data after exclusivity cuts (red), and the carbon data after exclusivity cuts (purple).

The π^0 background subtraction for the Fall2022 dataset DVCS analysis has not yet been completed. Instead, it was carried out for the FTon periods of RGC, and the value of the contamination as a function of ϕ as well as its impact on the target-spin asymmetry (TSA) is shown in Fig. 66. In the central ϕ region, which dominated by EC photons (same situation as RGH), where the

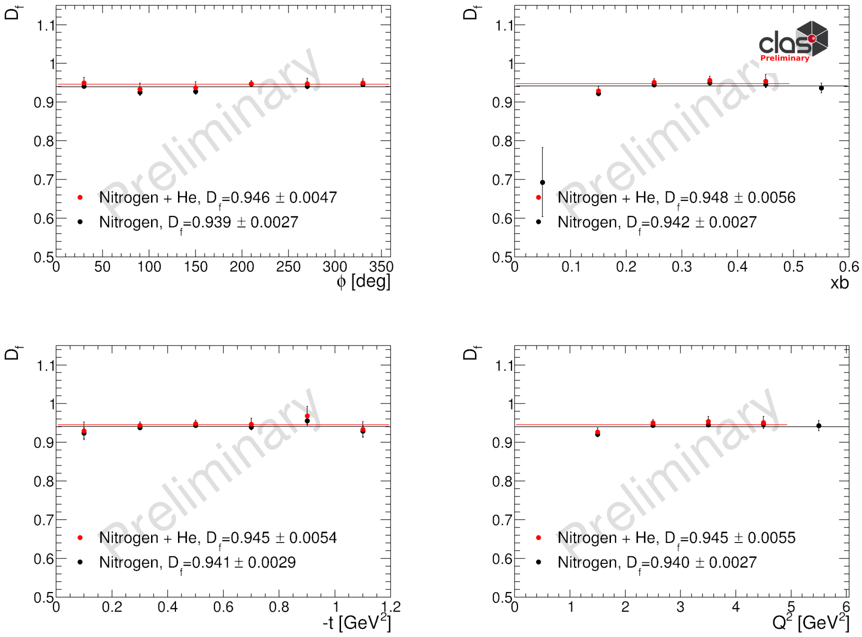

Fig. 65: Preliminary dilution factor for DVCS events, RGC Fall2022 data, as a function of ϕ (top left), x_B (top right), $-t$ (bottom left), Q^2 (bottom right). The black and red points correspond to two different methods to compute the dilution factor, and yield very similar results.

pi^0 cross section is high and the DVCS one is low, the π^0 background reaches 30%. However, its impact on the TSA appears minimal, due to the small size of the TSA for exclusive π^0 production compared to the DVCS.

6.3 Systematic uncertainties

Note that RGH presently assumes to run at a luminosity that is 20 times lower than the nominal CLAS12 value. As a consequence, the precision of the RGH results is expected to be statistically dominated, especially for DVCS.

At JLab, there is a consolidated knowledge of the NH_3 target polarization, which will only increase with the recent CLAS12 RGC run. When using NMR to measure the polarization of the NH_3 target, the typical uncertainty is 4-5%. The SANE experiment in Hall C (similar target geometry) quotes an uncertainty in the dilution factor of 2% [90].

The published analyses from CLAS/CLAS12 of SIDIS and DVCS observables present systematic uncertainties on acceptance and radiative corrections that are good references for RGH. Possible effects of the missing sector will be mitigated by the microwave-induced swap of the target polarization and are expected to not significantly increase the acceptance uncertainty because the CLAS12 acceptance is already not azymuthally uniform. The RGH recoil is based on technologies (MGPD tracking and scintillating materials) that are al-

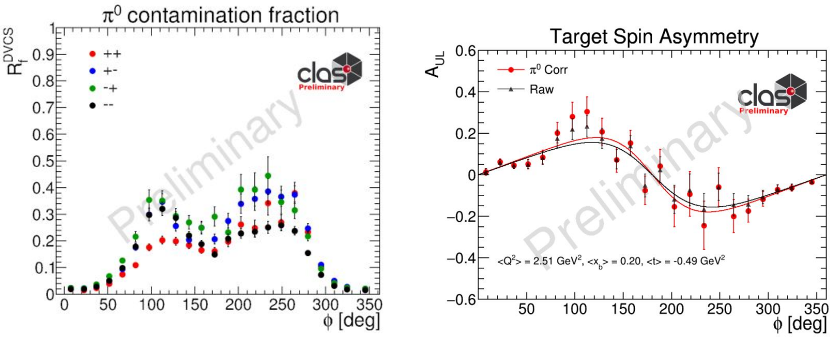

Fig. 66: Left: π^0 contamination on proton DVCS events, as a function of ϕ and for all combinations of spin of beam and target. Right: preliminary longitudinal targe-spin asymmetry for proton DVCS (RGC Summer2022 dataset), with and without π^0 subtraction.

ready in use at CLAS12. The effect of the recoil detector performance was studied varying resolution and kinematic range, and typical variations were found to be within 5%. Particle identification, accidental coincidences, and the photo-production of electrons that are misidentified as the scattered electron are typically found to be negligible. The main contributions to systematic uncertainties are listed, for the different reactions of interest, in Tables 5 to 7.

For DVCS, it is anticipated that the main source of systematic uncertainty will come from the choice of the exclusivity cuts. This has been observed in several previous DVCS analyses in CLAS and CLAS12. In the case of the polarized-target analysis, the exclusivity cuts serve the dual purpose of minimizing π^0 contamination as well as reducing the nuclear background from nitrogen. Following the results obtained in the published NH_3 CLAS DVCS analysis [47], we assume around 10% of systematic uncertainty associated to the choice of the exclusivity cuts. The π^0 subtraction will contribute to a few percent of systematic uncertainty, as was established in several previous DVCS analyses by changing the background-subtraction method. The 5% of uncertainty due to the performances of the recoil detector was estimated, as mentioned above, by studying the variation of the DVCS yields with varying detector resolutions.

Source	Systematic Uncertainty
Target polarization	5 %
Target dilution	2 %
Radiative effects	3 %
Acceptance and bin-migration	3 %

Tab. 5: Estimated main contributions to the systematic uncertainty for SIDIS single hadron.

Source	Systematic Uncertainty
Target polarization	5 %
Target dilution	2 %
Baryonic contribution from target fragmentation	1-6%
Bin migration close to ρ mass	1-10%

Tab. 6: Estimated main contributions to the systematic uncertainty for SIDIS di-hadron.

Source	Systematic Uncertainty
Target polarization	5 %
Target dilution	1 %
Recoil performances	5 %
π^0 background	3 %
Exclusivity cuts	10 %

Tab. 7: Estimated main contributions to the systematic uncertainty for DVCS.

7 Beam Time Request

The required days of data taking for the RGH physics and calibration runs are listed in Table 8. The days here discussed are calculated assuming the accelerator is available at all times with 100% of duty cycle.

To achieve the physics goals of the RGH experiments (according to the projections presented in Sec. 6), 100 days of physics data taking are required.

The run time with ancillary targets (^{12}C, CH_2 and Empty) accounts for 5 days of commissioning of the new elements (beam line, target, detector), and detector alignment runs. In addition, 8+2 days are required for background calibration, to correct target dilution due to heavy nuclear content.

The overhead for target operations is described in Sec. 4.1 and summarized here. Assuming 1 nA and raster diameter of 1.3 cm, each ammonia sample will last about 6 days of beam before annealing is necessary. With two interchangeable ammonia cells on the ladder and some days of background running, one would only need to anneal every 14 days and replace the samples after about 70–80 days (we assume twice). Annealing and polarization recovery will require about 4 h. Thermal equilibrium (TE) calibrations of the NMR instrumentation will be performed weekly and require 8 hours. The target replacement could take UP TO 24 h, depending on the final layout of the beam line. This amounts to 9 days of target overhead, plus 1 day of contingency.

8 Summary

The RGH experiments at CLAS12 offer a compelling physics program that has the potential to provide unprecedented information on the peculiar parton dynamics within the nucleon and during fragmentation. It will complement the information gathered with unpolarized and longitudinally polarized targets by the same experiment. Since the approval in 2012, the interest in this field of research has grown worldwide and culminated with the start of the EIC Project.

Beam Energy (GeV)	Beam Current (nA)	Beam Requirements	Target	Material Thickness (mg/cm^2)	Beamtime (days)
10.6	1	Polarized	NH_3	1040	100
10.6	1	Polarized	$^{12}C, CH_2$	1040, 1040	5+8
10.6	1	Polarized	Empty	na	2
			Operations		10
Total					125

Tab. 8: Data-taking time required to achieve the proposed physics goals assuming the accelerator is available at all times (100% duty cycle)

The theoretical understanding and lattice calculations have made important progresses, which consolidate the interest in new experimental results. At the same time, a comprehensive program has been pursued at JLab to understand and overcome the technical challenges connected with running a transversely polarized target inside CLAS12. The adopted solution is based on extended validation tests of target alternatives with electron beam, real data and concrete experience acquired so far running the experiment, and the choice of consolidated technologies to favor physics over development. CLAS12 is a running facility with the desired resolution, acceptance and particle identification capabilities validated, and with further potential upgrades being pursued that could boost the RGH reach. We request the PAC to approve the requested beam time (125 days).

References

[1] JLab PAC. PAC39 Report. *https://www.jlab.org/exp_prog/PACpage/PAC39/PAC39%20Final_Report.pdf*, 2012.

[2] JLab PAC. PAC41 High-Impact Selection. *https://www.jlab.org/exp_prog/PACpage/PAC41/PAC41_Report.pdf*, 2014.

[3] H. Avakian et al. Transverse spin effects in SIDIS at 11 GeV with a transversely polarized target using the CLAS12 Detector. *https://www.jlab.org/exp_prog/proposals/12/C12-11-111.pdf*, 2012.

[4] H. Avakian et al. Measurement of transversity with dihadron production in SIDIS with transversely polarized target. *https://www.jlab.org/exp_prog/proposals/12/PR12-12-009.pdf*, 2012.

[5] H. Avakian et al. Deeply Virtual Compton Scattering at 11 GeV with transversely polarized target using the CLAS12 Detector. *https://www.jlab.org/exp_prog/proposals/12/PR12-12-010_rv.pdf*, 2012.

[6] A. Accardi et al. Electron Ion Collider: The Next QCD Frontier: Understanding the glue that binds us all. *Eur. Phys. J. A*, 52(9):268, 2016.

[7] R. Abdul Khalek et al. Science Requirements and Detector Concepts for the Electron-Ion Collider: EIC Yellow Report. *Nucl. Phys. A*, 1026:122447, 2022.

[8] JLab PAC. PAC52 Report. *https://www.jlab.org/sites/default/files/PAC/PAC52/PAC52%20REPORT%202024.pdf*, 2024.

[9] C. Lorce and B. Pasquini. Quark Wigner Distributions and Orbital Angular Momentum. *Phys. Rev. D*, 84:014015, 2011.

[10] Matthias Burkardt. Chromodynamic lensing and transverse single spin asymmetries. *Nucl. Phys. A*, 735:185–199, 2004.

[11] Alessandro Bacchetta and Marco Radici. Constraining quark angular momentum through semi-inclusive measurements. *Phys. Rev. Lett.*, 107:212001, 2011.

[12] L. Gamberg, M. Malda, J.A. Miller, D. Pitonyak, A. Prokudin, and N. Sato. Updated QCD global analysis of single transverse-spin asymmetries: Extracting $\tilde{\mathrm{H}}$, and the role of the Soffer bound and lattice QCD. *Phys. Rev. D*, 106(3):034014, 2022.

[13] Zhong-Bo Kang, Alexei Prokudin, Peng Sun, and Feng Yuan. Extraction of Quark Transversity Distribution and Collins Fragmentation Functions with QCD Evolution. *Phys. Rev. D*, 93(1):014009, 2016.

[14] M. Anselmino, M. Boglione, U. D'Alesio, S. Melis, F. Murgia, and A. Prokudin. Simultaneous extraction of transversity and Collins functions from new SIDIS and e+e- data. *Phys. Rev. D*, 87:094019, 2013.

[15] M. Anselmino, M. Boglione, U. D'Alesio, J. O. Gonzalez Hernandez, S. Melis, F. Murgia, and A. Prokudin. Collins functions for pions from SIDIS and new e^+e^- data: a first glance at their transverse momentum dependence. *Phys. Rev. D*, 92(11):114023, 2015.

[16] Umberto D'Alesio, Carlo Flore, and Alexei Prokudin. Role of the Soffer bound in determination of transversity and the tensor charge. *Phys. Lett. B*, 803:135347, 2020.

[17] Marco Radici and Alessandro Bacchetta. First Extraction of Transversity from a Global Analysis of Electron-Proton and Proton-Proton Data. *Phys. Rev. Lett.*, 120(19):192001, 2018.

[18] J. Benel, A. Courtoy, and R. Ferro-Hernandez. A constrained fit of the valence transversity distributions from dihadron production. *Eur. Phys. J. C*, 80(5):465, 2020.

[19] Huey-Wen Lin, W. Melnitchouk, Alexei Prokudin, N. Sato, and H. Shows. First Monte Carlo Global Analysis of Nucleon Transversity with Lattice QCD Constraints. *Phys. Rev. Lett.*, 120(15):152502, 2018.

[20] Justin Cammarota, Leonard Gamberg, Zhong-Bo Kang, Joshua A. Miller, Daniel Pitonyak, Alexei Prokudin, Ted C. Rogers, and Nobuo Sato. Origin of single transverse-spin asymmetries in high-energy collisions. *Phys. Rev. D*, 102(5):054002, 2020.

[21] M. Boglione, U. D'Alesio, C. Flore, J.O. Gonzalez-Hernandez, F. Murgia, and A. Prokudin. Simultaneous reweighting of Transverse Momentum Dependent distributions. *Phys. Lett. B*, 854:138712, 2024.

[22] C. Cocuzza, A. Metz, D. Pitonyak, A. Prokudin, N. Sato, and R. Seidl. First simultaneous global QCD analysis of dihadron fragmentation functions and transversity parton distribution functions. *Phys. Rev. D*, 109(3):034024, 2024.

[23] C. Cocuzza, A. Metz, D. Pitonyak, A. Prokudin, N. Sato, and R. Seidl. Transversity Distributions and Tensor Charges of the Nucleon: Extraction from Dihadron Production and Their Universal Nature. *Phys. Rev. Lett.*, 132(9):091901, 2024.

[24] H. Avakian, A. Bressan, and M. Contalbrigo. Experimental results on TMDs. *Eur. Phys. J. A*, 52(6):150, 2016. [Erratum: Eur.Phys.J.A 52, 165 (2016)].

[25] Marco Radici, A. Courtoy, Alessandro Bacchetta, and Marco Guagnelli. Improved extraction of valence transversity distributions from inclusive dihadron production. *JHEP*, 05:123, 2015.

[26] Rajan Gupta, Yong-Chull Jang, Boram Yoon, Huey-Wen Lin, Vincenzo Cirigliano, and Tanmoy Bhattacharya. Isovector Charges of the Nucleon from 2+1+1-flavor Lattice QCD. *Phys. Rev. D*, 98:034503, 2018.

[27] Rajan Gupta, Boram Yoon, Tanmoy Bhattacharya, Vincenzo Cirigliano, Yong-Chull Jang, and Huey-Wen Lin. Flavor diagonal tensor charges of the nucleon from (2+1+1)-flavor lattice QCD. *Phys. Rev. D*, 98(9):091501, 2018.

[28] C. Alexandrou, S. Bacchio, M. Constantinou, J. Finkenrath, K. Hadjiyiannakou, K. Jansen, G. Koutsou, and A. Vaquero Aviles-Casco. Nucleon axial, tensor, and scalar charges and σ-terms in lattice QCD. *Phys. Rev. D*, 102(5):054517, 2020.

[29] M. Pitschmann, C.-Y. Seng, C.D. Roberts, and S.M. Schmidt. Nucleon tensor charges and electric dipole moments. *Phys. Rev. D*, 91:074004, 2015.

[30] A. Courtoy, S. Baeßler, M. González-Alonso, and S. Liuti. Beyond-Standard-Model Tensor Interaction and Hadron Phenomenology. *Phys. Rev. Lett.*, 115:162001, 2015.

[31] A. Bacchetta, D. Boer, M. Diehl, and P.J. Mulders. Matches and mismatches in the descriptions of semi-inclusive processes at low and high transverse momentum. *JHEP*, 08:023, 2008.

[32] I. Garzia and F. Giordano. Transverse-momentum-dependent fragmentation functions in e^+e^- annihilation. *Eur. Phys. J. A*, 52(6):152, 2016.

[33] M.J. Skoby. High Precision Measurement of Transversity Using Di-hadron Correlations in $p^\uparrow + p$ Collisions at $\sqrt{s_{NN}} = 500$ GeV. *Int. J. Mod. Phys. Conf. Ser.*, 40:1660038, 2016.

[34] D. Müller, D. Robaschik, B. Geyer, F.-M. Dittes, and J. Hořejši. Wave functions, evolution equations and evolution kernels from light-ray operators of qcd. *Fortschritte der Physik/Progress of Physics*, 42(2):101–141, 1994.

[35] X.-D. Ji. Gauge-Invariant Decomposition of Nucleon Spin. *Phys. Rev. Lett.*, 78:610–613, 1997.

[36] A. V. Radyushkin. Nonforward parton distributions. *Phys. Rev. D*, 56:5524–5557, Nov 1997.

[37] John C. Collins, Leonid Frankfurt, and Mark Strikman. Factorization for hard exclusive electroproduction of mesons in qcd. *Phys. Rev. D*, 56:2982–3006, Sep 1997.

[38] K. Goeke, M.V. Polyakov, and M. Vanderhaeghen. Hard exclusive reactions and the structure of hadrons. *Progress in Particle and Nuclear Physics*, 47(2):401–515, 2001.

[39] M. Diehl. Generalized parton distributions. *Physics Reports*, 388(2):41–277, 2003.

[40] A.V. Belitsky and A.V. Radyushkin. Unraveling hadron structure with generalized parton distributions. *Physics Reports*, 418(1):1–387, 2005.

[41] M. Guidal. A fitter code for deep virtual compton scattering and generalized parton distributions. *The European Physical Journal A*, 37(3):319–332, September 2008.

[42] S. Stepanyan et al. Observation of exclusive deeply virtual compton scattering in polarized electron beam asymmetry measurements. *Phys. Rev. Lett.*, 87:182002, Oct 2001.

[43] C. Munoz Camacho et al. Scaling tests of the cross section for deeply virtual compton scattering. *Phys. Rev. Lett.*, 97:262002, Dec 2006.

[44] F. X. Girod et al. Measurement of deeply virtual compton scattering beam-spin asymmetries. *Phys. Rev. Lett.*, 100:162002, Apr 2008.

[45] S. Chen et al. Measurement of deeply virtual compton scattering with a polarized-proton target. *Phys. Rev. Lett.*, 97:072002, Aug 2006.

[46] E. Seder et al. Longitudinal target-spin asymmetries for deeply virtual compton scattering. *Phys. Rev. Lett.*, 114:032001, Jan 2015.

[47] S. Pisano et al. Single and double spin asymmetries for deeply virtual compton scattering measured with clas and a longitudinally polarized proton target. *Phys. Rev. D*, 91:052014, Mar 2015.

[48] H. S. Jo et al. Cross sections for the exclusive photon electroproduction on the proton and generalized parton distributions. *Phys. Rev. Lett.*, 115:212003, Nov 2015.

[49] M. Defurne et al. E00-110 experiment at jefferson lab hall a: Deeply virtual compton scattering off the proton at 6 gev. *Phys. Rev. C*, 92:055202, Nov 2015.

[50] G. Christiaens et al. First clas12 measurement of deeply virtual compton scattering beam-spin asymmetries in the extended valence region. *Phys. Rev. Lett.*, 130:211902, May 2023.

[51] A. Airapetian et al. Measurement of the beam-spin azimuthal asymmetry associated with deeply-virtual compton scattering. *Phys. Rev. Lett.*, 87:182001, Oct 2001.

[52] A. Airapetian et al. Beam-charge azimuthal asymmetry and deeply virtual compton scattering. *Phys. Rev. D*, 75:011103, Jan 2007.

[53] A. Airapetian et al. Measurement of Azimuthal Asymmetries With Respect To Both Beam Charge and Transverse Target Polarization in Exclusive Electroproduction of Real Photons. *JHEP*, 06:066, 2008.

[54] A. Airapetian et al. Separation of contributions from deeply virtual Compton scattering and its interference with the Bethe-Heitler process in measurements on a hydrogen target. *JHEP*, 11:083, 2009.

[55] A. Airapetian et al. Exclusive Leptoproduction of Real Photons on a Longitudinally Polarised Hydrogen Target. *JHEP*, 06:019, 2010.

[56] A. Airapetian et al. Measurement of double-spin asymmetries associated with deeply virtual Compton scattering on a transversely polarized hydrogen target. *Phys. Lett.*, B704:15–23, 2011.

[57] A. Airapetian et al. Beam-helicity and beam-charge asymmetries associated with deeply virtual Compton scattering on the unpolarised proton. *JHEP*, 07:032, 2012.

[58] F. D. Aaron et al. Measurement of Diffractive Scattering of Photons with Large Momentum Transfer at HERA. *Phys. Lett. B*, 672:219–226, 2009.

[59] A. Aktas et al. Measurement of deeply virtual compton scattering at HERA. *Eur. Phys. J.*, C44:1–11, 2005.

[60] C. Adloff et al. Measurement of deeply virtual Compton scattering at HERA. *Phys. Lett.*, B517:47–58, 2001.

[61] S. Chekanov et al. A Measurement of the Q**2, W and t dependences of deeply virtual Compton scattering at HERA. *JHEP*, 05:108, 2009.

[62] S. Chekanov et al. Measurement of deeply virtual Compton scattering at HERA. *Phys. Lett.*, B573:46–62, 2003.

[63] R. Akhunzyanov et al. Transverse extension of partons in the proton probed in the sea-quark range by measuring the dvcs cross section. *Physics Letters B*, 793:188–194, 2019.

[64] Andrei V. Belitsky, Dieter Mueller, and A. Kirchner. Theory of deeply virtual Compton scattering on the nucleon. *Nucl. Phys.*, B629:323–392, 2002.

[65] C. Alexandrou. Recent progress on the study of nucleon structure from lattice QCD and future perspectives. *SciPost Phys. Proc.*, 3:015, 2020.

[66] A. Bacchetta, M. Diehl, K. Goeke, A. Metz, P.J. Mulders, and M. Schlegel. Semi-inclusive deep inelastic scattering at small transverse momentum. *JHEP*, 02:093, 2007.

[67] S.V. Goloskokov and P. Kroll. Transversity in hard exclusive electroproduction of pseudoscalar mesons. *Eur. Phys. J. A*, 47:112, 2011.

[68] S.V. Goloskokov and P. Kroll. An Attempt to understand exclusive pi+ electroproduction. *Eur. Phys. J. C*, 65:137–151, 2010.

[69] G.D. Alexeev et al. Transverse-spin-dependent azimuthal asymmetries of pion and kaon pairs produced in muon-proton and muon-deuteron semi-inclusive deep inelastic scattering. *Phys. Lett. B*, 845:138155, 2023.

[70] G.D. Alexeev et al. High-Statistics Measurement of Collins and Sivers Asymmetries for Transversely Polarized Deuterons. *Phys. Rev. Lett.*, 133(10):101903, 2024.

[71] A. Airapetian et al. Azimuthal single- and double-spin asymmetries in semi-inclusive deep-inelastic lepton scattering by transversely polarized protons. *JHEP*, 12:010, 2020.

[72] M.G. Alexeev et al. Measurement of P_T-weighted Sivers asymmetries in leptoproduction of hadrons. *Nucl. Phys. B*, 940:34–53, 2019.

[73] G.D. Alexeev et al. Final COMPASS Results on the Transverse-Spin-Dependent Azimuthal Asymmetries in the Pion-Induced Drell-Yan Process. *Phys. Rev. Lett.*, 133(7):071902, 2024.

[74] C. Alexandrou et al. Moments of the nucleon transverse quark spin densities using lattice QCD. *Phys. Rev. D*, 107(5):054504, 2023.

[75] A. Scapellato, C. Alexandrou, K. Cichy, M. Constantinou, K. Hadjiyiannakou, K. Jansen, and F. Steffens. Proton generalized parton distributions from lattice QCD. *Rev. Mex. Fis. Suppl.*, 3(3):0308104, 2022.

[76] H. Gao et al. Target Single Spin Asymmetry in Semi-Inclusive Deep-Inelastic $(e, e'^{\pm})$ Reaction on a Transversely Polarized ^{3}He Target at 8.8 and 11 GeV - E12-10-006. *https://www.jlab.org/exp_prog/proposals/10/PR12-10-006.pdf*, 2010.

[77] H. Gao et al. Target Single Spin Asymmetry in Semi-Inclusive Deep-Inelastic $(e, e'^{\pm})$ Reaction on a Transversely Polarized Proton Target - E12-11-108. *https://www.jlab.orgexp_progproposals11PR12-11-108.pdf*, 2011.

[78] O. Bessidskaia Bylund, M. Defurne, and P.A.M. Guichon. Recoil proton polarization: A new discriminative observable for deeply virtual Compton scattering. *Phys. Rev. D*, 107(1):014020, 2023.

[79] M. Defurne et al. Recoil Nucleon Polarization in Deeply Virtual Compton Scattering and Neutral Pion Electroproduction in Hall-C - LOI12-23-014. *https:www.jlab.orgexp_progproposals23LOI12-23-014.pdf*, 2023.

[80] M. Čuić, K. Kumerički, and A. Schäfer. Separation of Quark Flavors Using Deeply Virtual Compton Scattering Data. *Phys. Rev. Lett.*, 125(23):232005, 2020.

[81] F. Georges et al. Deeply Virtual Compton Scattering Cross Section at High Bjorken xB. *Phys. Rev. Lett.*, 128(25):252002, 2022.

[82] P.A. Adderley et al. The Continuous Electron Beam Accelerator Facility at 12 GeV. *Phys. Rev. Accel. Beams*, 27(8):084802, 2024.

[83] V.D. Burkert et al. The CLAS12 Spectrometer at Jefferson Laboratory. *Nucl. Instrum. Meth. A*, 959:163419, 2020.

[84] B. Raydo, S. Boyarinov, A. Celentano, C. Cuevas, R. de Vita, V. Kubarovsky, B. Moffit, S. Niccolai, R. Paremuzyan, and C. Smith. The CLAS12 Trigger System. *Nucl. Instrum. Meth. A*, 960:163529, 2020.

[85] D.S. Carman et al. The CLAS12 Forward Time-of-Flight system. *Nucl. Instrum. Meth. A*, 960:163629, 2020.

[86] M. Contalbrigo et al. The large-area hybrid-optics CLAS12 RICH: First years of data-taking. *Nucl. Instrum. Meth. A*, 1057:168758, 2023.

[87] M. Contalbrigo et al. The CLAS12 Ring Imaging Cherenkov detector. *Nucl. Instrum. Meth. A*, 964:163791, 2020.

[88] J. Pierce, J. Maxwell, and C. Keith. Dynamically polarized target for the g_2^p and G_E^p experiments at Jefferson Lab. *Nucl. Instrum. Meth. A*, 738:54–60, 2014.

[89] Christopher Keith. A Dynamically Polarized Solid Target for CLAS12. *PoS*, PSTP2017:008, 2018.

[90] J. D. Maxwell et al. Design and Performance of the Spin Asymmetries of the Nucleon Experiment. *Nucl. Instrum. Meth. A*, 885:145–159, 2018.

[91] C. D. Keith, J. Brock, C. Carlin, T. Kageya, V. Lagerquist, J. Maxwell, and P. Pandey. First Use of a Longitudinally Polarized Target with CLAS12. *PoS*, PSTP2022:009, 2023.

[92] Christopher Keith. Design Considerations for a Transversely Polarized Solid Target in Hall B at Jefferson Lab. *PoS*, SPIN2023:214, 2024.

[93] CryoMagnetics Inc. 7.5 Tesla Split Pair Cryogen-FREE Magnet System Dual RTB. *https://cryomagnetics.com/7-5-tesla-split-pair-cryogen-free-magnet-system-dual-rtb/*, 2025.

[94] M. Böhm, A. Lehmann, S. Motz, and F. Uhlig. Fast SiPM Readout of the PANDA TOF Detector. *JINST*, 11(05):C05018, 2016.

[95] T. Rostomyan et al. Timing detectors with SiPM read-out for the MUSE experiment at PSI. *Nucl. Instrum. Meth. A*, 986:164801, 2021.

[96] F. Sauli. GEM: A new concept for electron amplification in gas detectors. *Nucl. Instrum. Meth. A*, 386:531–534, 1997.

[97] L. Periale, V. Peskov, P. Carlson, T. Francke, P. Pavlopoulos, P. Picchi, and F. Pietropaolo. Detection of the primary scintillation light from dense Ar, Kr and Xe with novel photosensitive gaseous detectors. *Nucl. Instrum. Meth. A*, 478:377–383, 2002.

[98] R. Chechik, A. Breskin, and C. Shalem. Thick GEM-like multipliers: A Simple solution for large area UV-RICH detectors. *Nucl. Instrum. Meth. A*, 553:35–40, 2005.

[99] Y. Giomataris, P. Rebourgeard, J. P. Robert, and Georges Charpak. MICROMEGAS: A High granularity position sensitive gaseous detector for high particle flux environments. *Nucl. Instrum. Meth. A*, 376:29–35, 1996.

[100] G. Bencivenni, R. De Oliveira, G. Morello, and M. Poli Lener. The micro-Resistive WELL detector: a compact spark-protected single amplification-stage MPGD. *JINST*, 10(02):P02008, 2015.

[101] G. Bencivenni, R. De Oliveira, G. Felici, M. Gatta, M. Giovannetti, G. Morello, and M. Poli Lener. The μ-RWELL for high rate application. *JINST*, 15(09):C09034, 2020.

[102] M.J. French et al. Design and results from the APV25, a deep sub-micron CMOS front-end chip for the CMS tracker. *Nucl. Instrum. Meth. A*, 466:359–365, 2001.

[103] F. Dubinin, N. Boyko, A. Konotop, G. Dolganov, and A. Zhurkina. PET Prototype Based on Scintillation Detectors GAGG-SiPM Coupled to 32-Channel Petiroc2A Chip. *Phys. Part. Nucl. Lett.*, 21(4):715–718, 2024.

[104] T. Saleem, S. Ahmad, J.-B. Cizel, C. De La Taille, M. Morenas, V. Nadig, F. Perez, V. Schulz, S. Gundacker, and J. Fleury. Study experimental time resolution limits of recent ASICs at Weeroc with different SiPMs and scintillators. *JINST*, 18(10):P10005, 2023.

[105] R. Kelleher. A MuID and Hadronic Calorimeter for a Second Detector at the EIC - Talk at the 2024 Fall Meeting of the APS Division of Nuclear Physics. *https://meetings.aps.org/Meeting/DNP24/Session/F12.6*, 2012.

[106] P. Thomadakis, A. Angelopoulos, G. Gavalian, and N. Chrisochoides. Using machine learning for particle track identification in the CLAS12 detector. *Comput. Phys. Commun.*, 276:108360, 2022.

[107] P. Thomadakis, A. Angelopoulos, G. Gavalian, and N. Chrisochoides. De-noising drift chambers in CLAS12 using convolutional auto encoders. *Comput. Phys. Commun.*, 271:108201, 2022.

[108] G. Christiaens et al. First CLAS12 Measurement of Deeply Virtual Compton Scattering Beam-Spin Asymmetries in the Extended Valence Region. *Phys. Rev. Lett.*, 130(21):211902, 2023.

[109] T. B. Hayward et al. Observation of Beam Spin Asymmetries in the Process $ep \to e^{'}\pi^+\pi^-X$ with CLAS12. *Phys. Rev. Lett.*, 126:152501, 2021.

[110] S. Diehl et al. Multidimensional, High Precision Measurements of Beam Single Spin Asymmetries in Semi-inclusive π^+ Electroproduction off Protons in the Valence Region. *Phys. Rev. Lett.*, 128(6):062005, 2022.

[111] M. Anselmino, A. Mukherjee, and A.1 Vossen. Transverse spin effects in hard semi-inclusive collisions. *Prog. Part. Nucl. Phys.*, 114:103806, 2020.

[112] H.H. Matevosyan, A. Kotzinian, E.-C. Aschenauer, H. Avakian, and A.W. Thomas. Predictions for Sivers single spin asymmetries in one- and two-hadron electroproduction at CLAS12 and EIC. *Phys. Rev. D*, 92(5):054028, 2015.

[113] Y. Sawaya. Phenomenological fits of di-hadron $\mathrm{A_{UT}}$. *poster at POETIC Conference*, 2025.

[114] A. Airapetian et al. Measurement of Azimuthal Asymmetries With Respect To Both Beam Charge and Transverse Target Polarization in Exclusive Electroproduction of Real Photons. *JHEP*, 06:066, 2008.

[115] S Polcher et al. Release note: Dvcs on longitudinally polarised proton with the rgc experiment at clas12. 2025.